Figure 1.

This is the author manuscript accepted for publication and has undergone full peer review but has not been through the copyediting, typesetting, pagination and proofreading process, which may lead to differences between this version and the Version of Record. Please cite this article as doi: 10.1029/2018JA025543

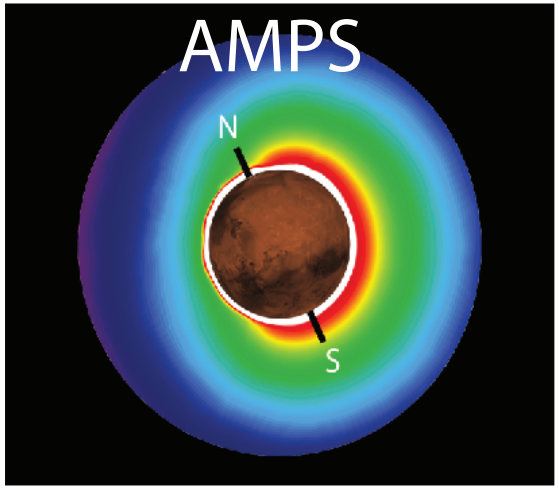

$[O_{hot}]$

$[O],[CO_2],[CO],$
$[N_2],[O_2^+],$
$[e^-],T_e,T_i,T_n,$
U_n,V_n,W_n

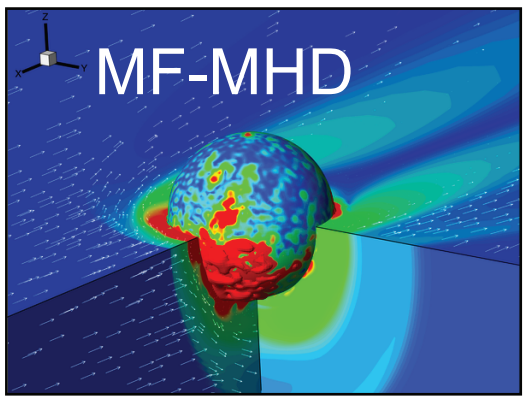

$[O],[CO_2],T_n,$
Ionization frequencies
$(CO_2 \rightarrow CO_2^+, O \rightarrow O^+, CO_2 \rightarrow O^+)$

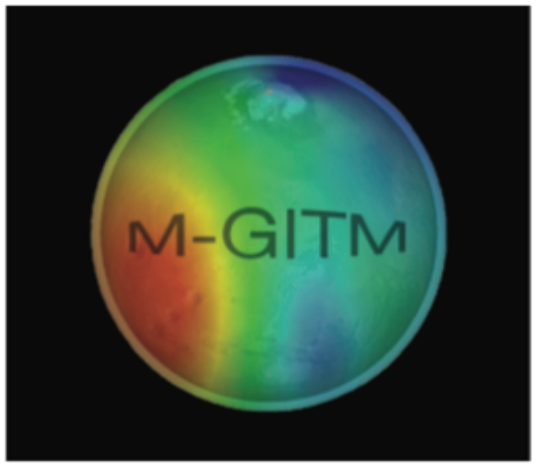

Figure 2.

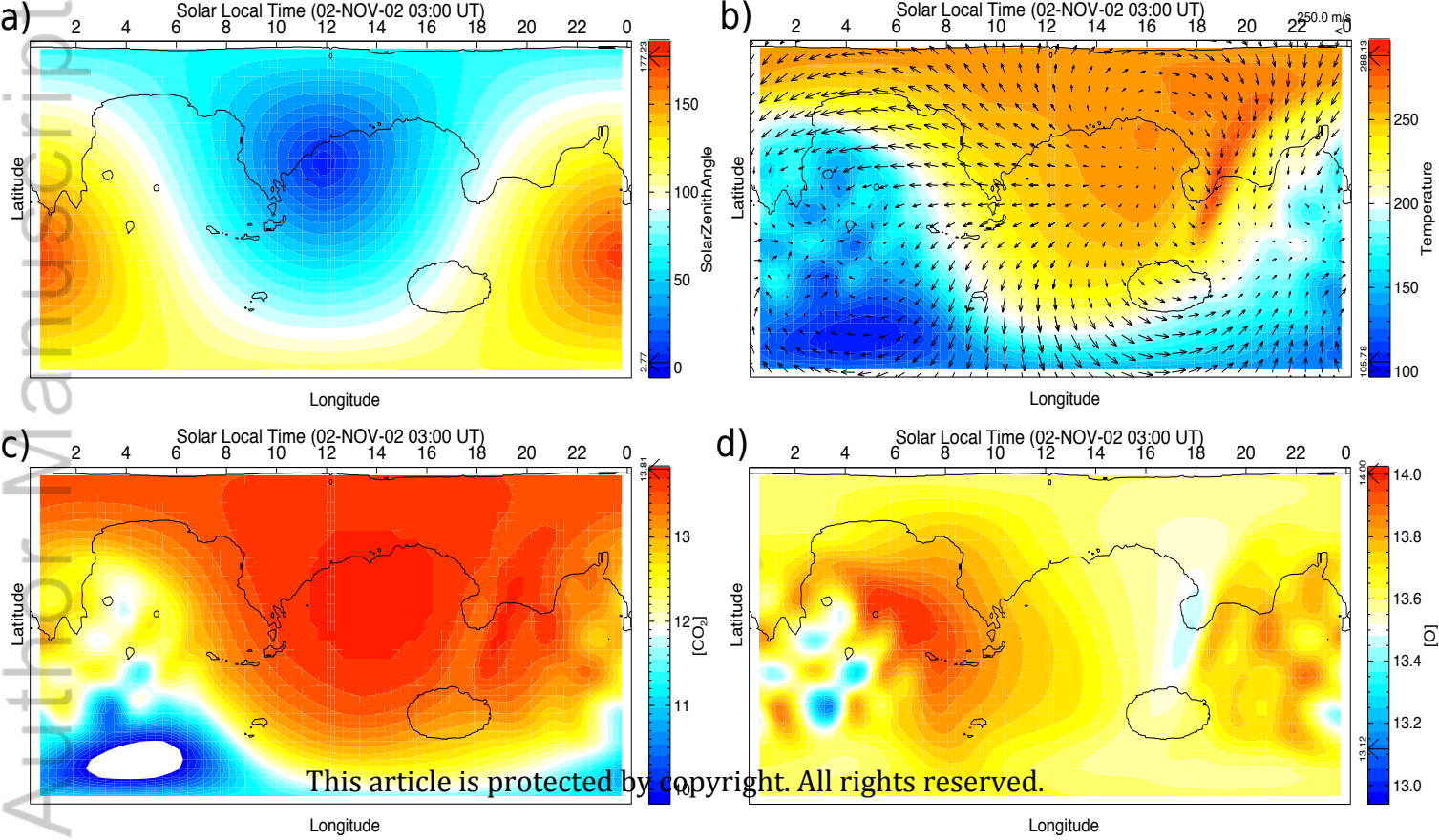

Figure 3.

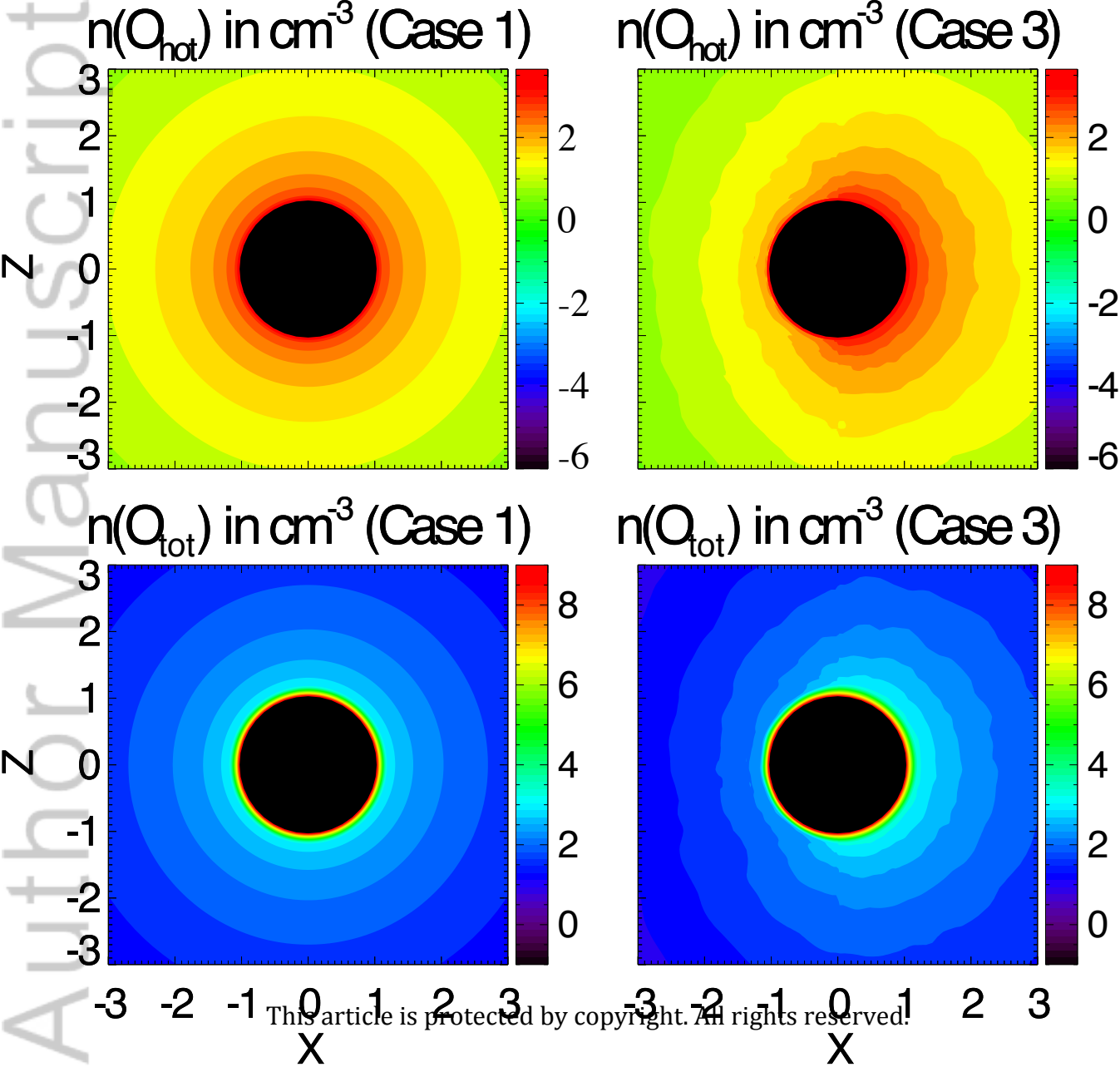

Figure 4.

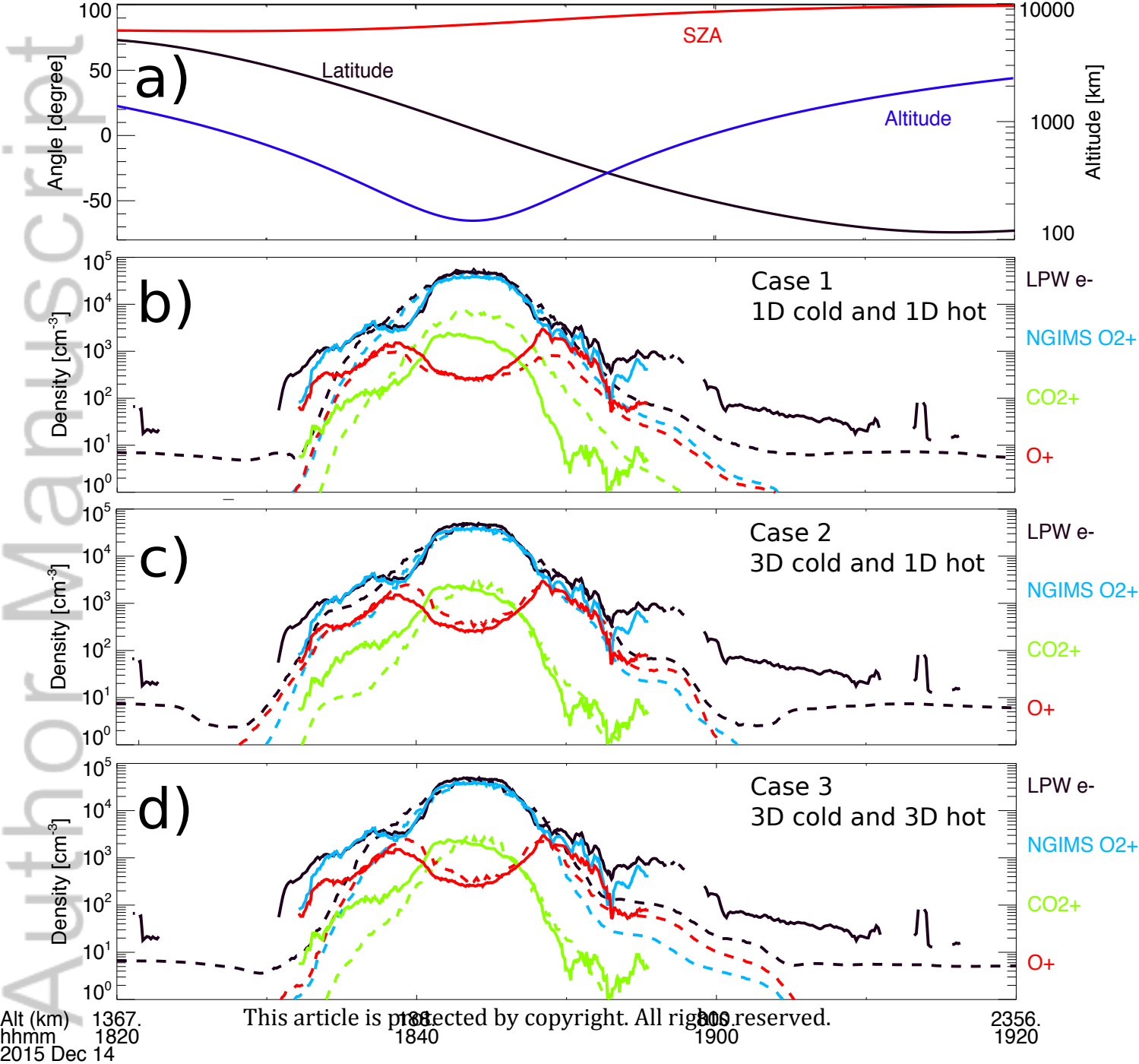

Figure 5.

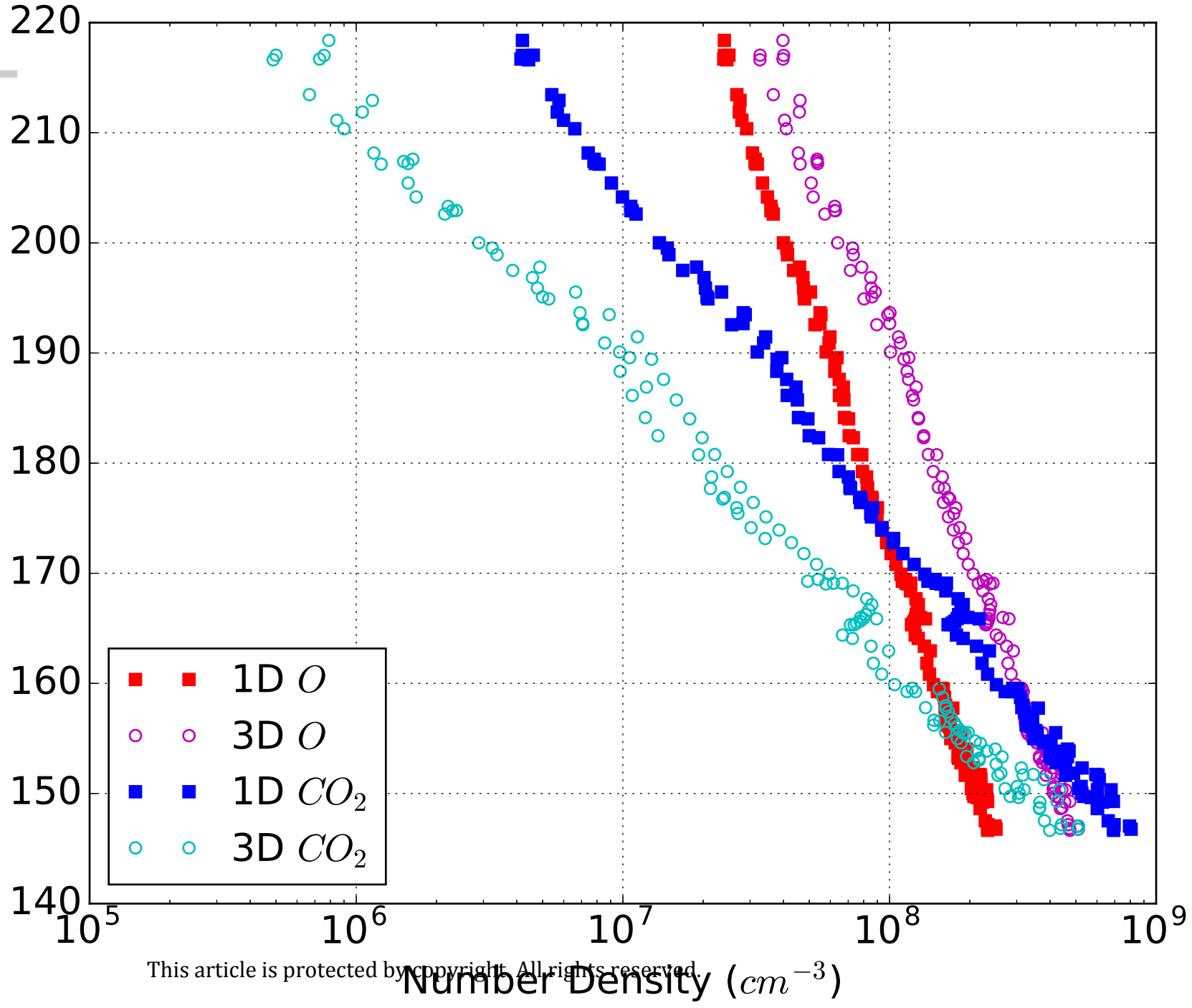

Figure 6.

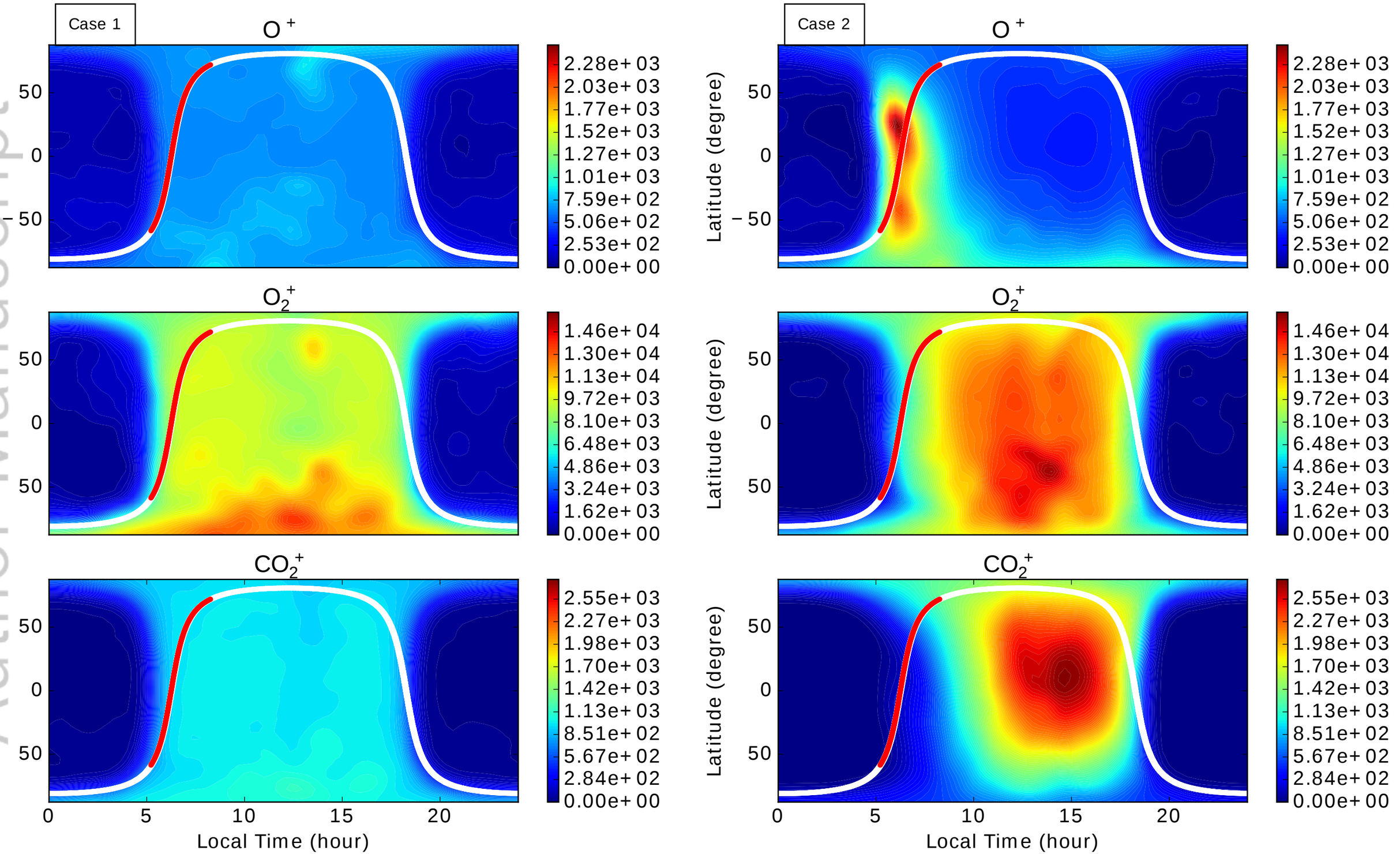

Figure 7.

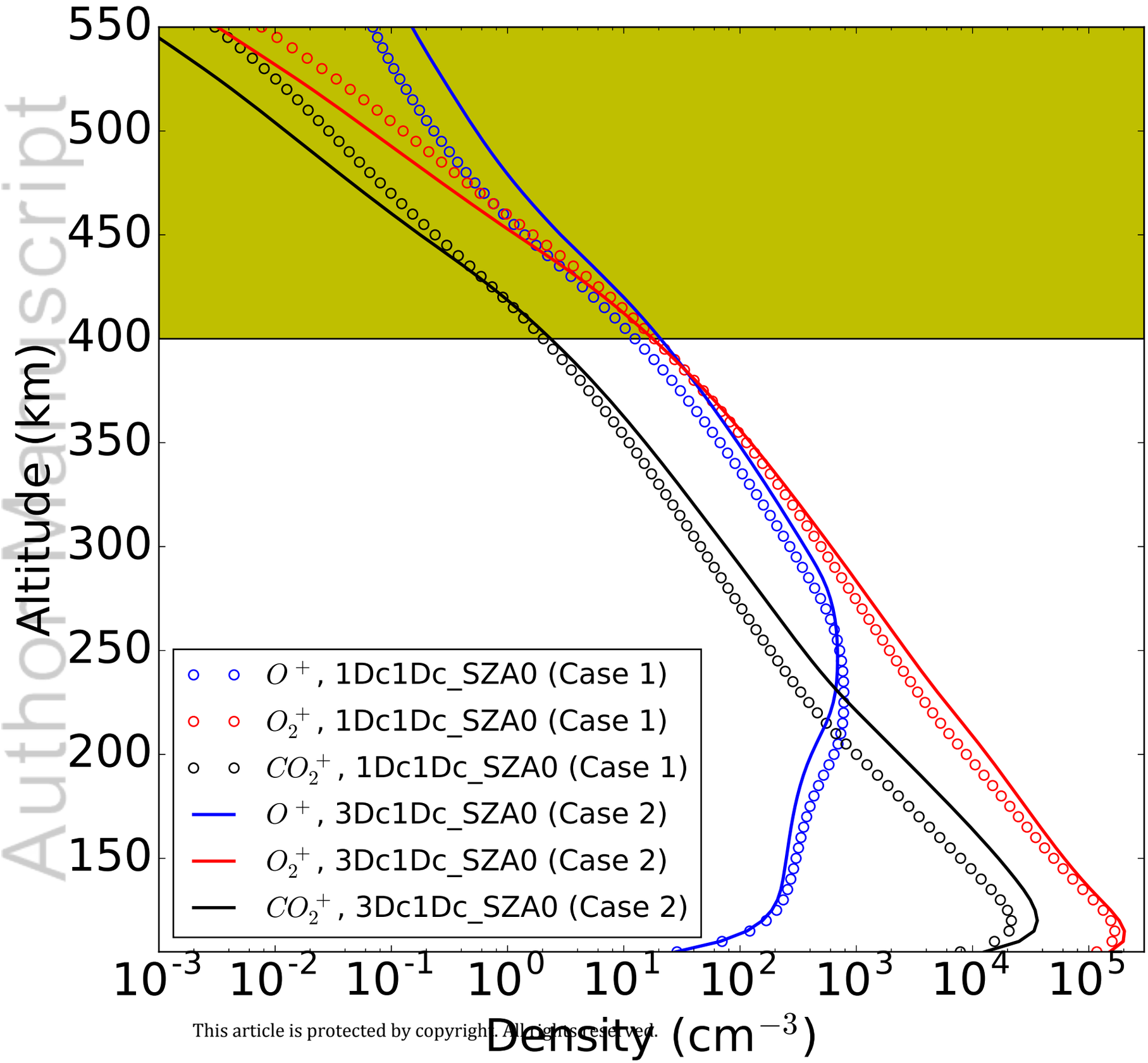

Figure 8.

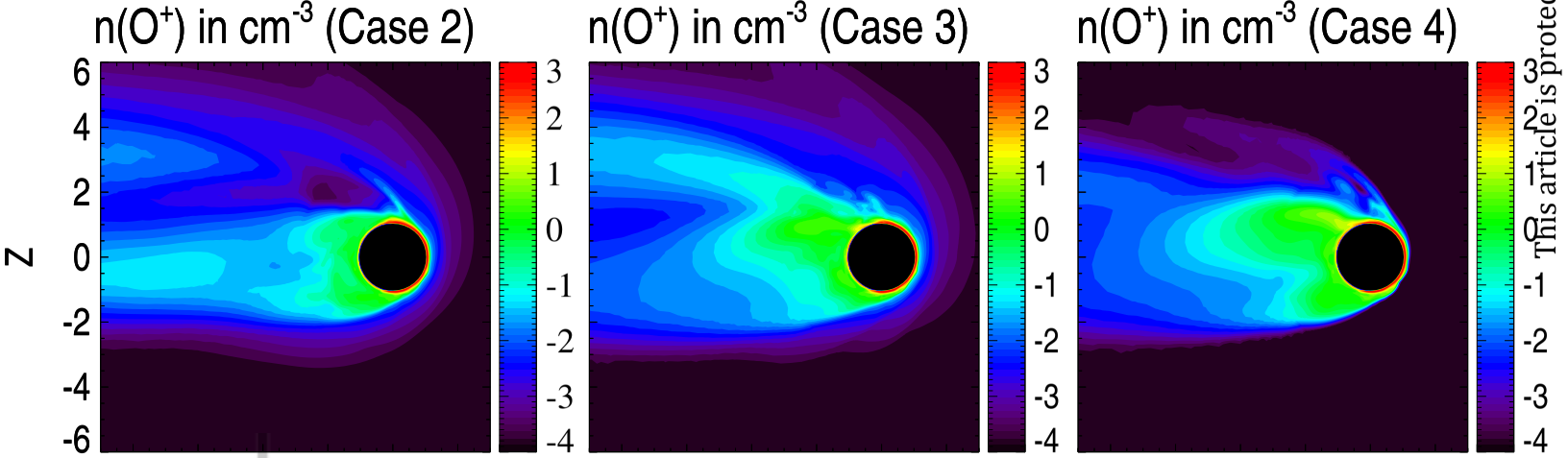

Figure 9.

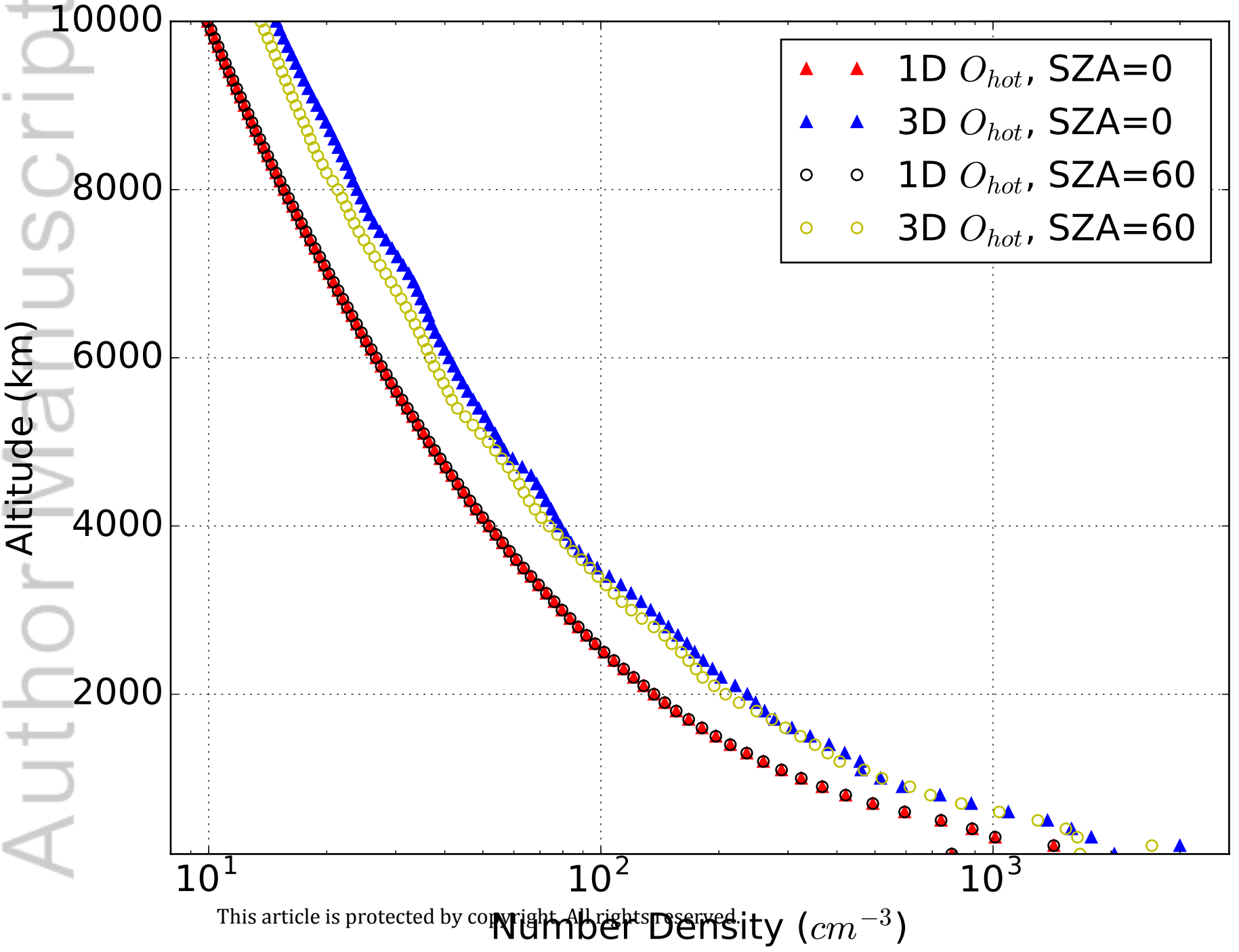

Figure 10.

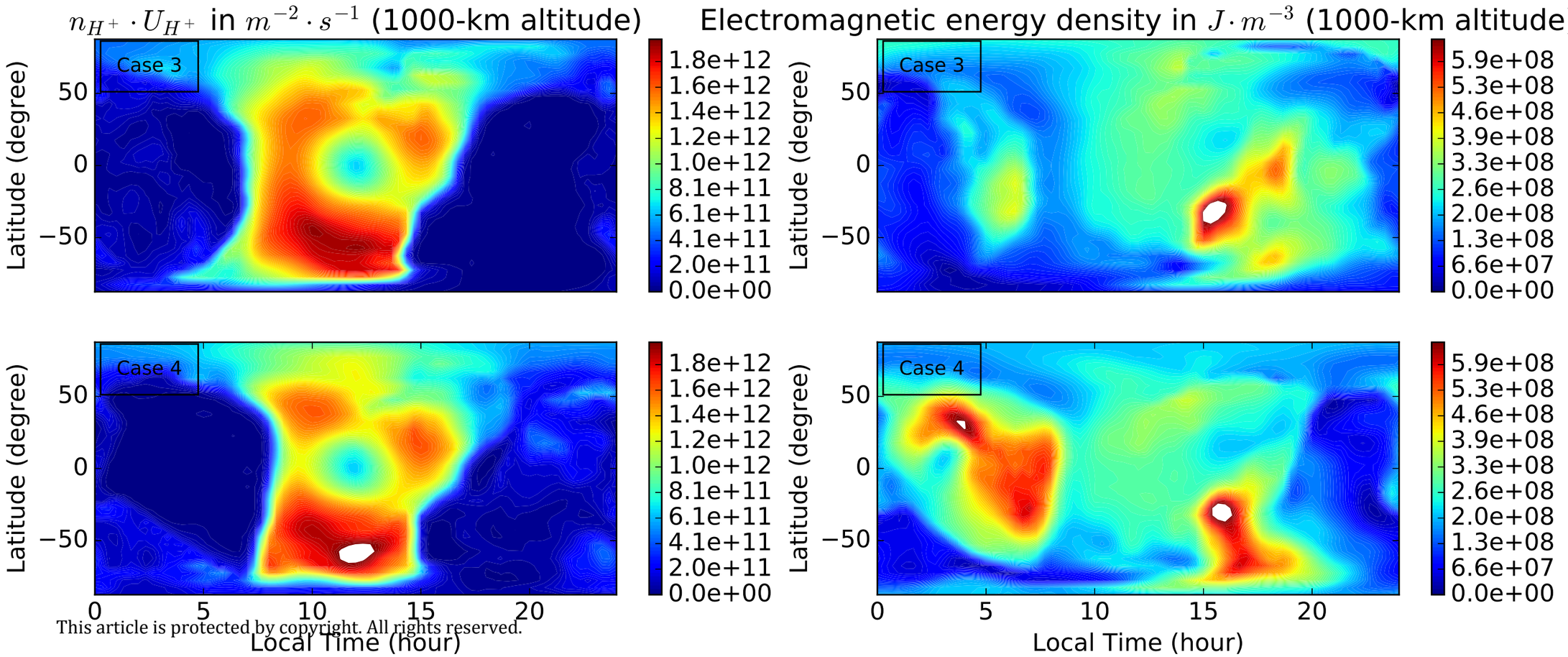

Solar wind interaction with the Martian upper atmosphere: Roles of the cold thermosphere and hot oxygen corona

Chuanfei Dong,[1,2] Stephen W. Bougher,[3] Yingjuan Ma,[4] Yuni Lee,[5] Gabor Toth,[3] Andrew F. Nagy,[3] Xiaohua Fang,[6] Janet Luhmann,[7] Michael W. Liemohn,[3] Jasper S. Halekas,[8] Valeriy Tenishev,[3] David J. Pawlowski,[9] Michael R. Combi[3]

[1]Department of Astrophysical Sciences, Princeton University, Princeton, New Jersey, USA
[2]Princeton Center for Heliophysics, Princeton Plasma Physics Laboratory, Princeton University, Princeton, New Jersey, USA
[3]Department of Climate and Space Sciences and Engineering, University of Michigan, Ann Arbor, Michigan, USA.
[4]Department of Earth and Space Sciences, University of California, Los Angeles, California, USA.
[5]NASA Goddard Space Flight Center, Greenbelt, Maryland, USA.
[6]Laboratory for Atmospheric and Space Physics, University of Colorado, Boulder, Colorado, USA.
[7]Space Sciences Laboratory, University of California, Berkeley, California, USA.
[8]Department of Physics and Astronomy, University of Iowa, Iowa City, Iowa, USA.
[9]Department of Physics and Astronomy, Eastern Michigan University, Ypsilanti, Michigan, USA.

Key Points:

- Despite the similar ion loss rate calculated from 1D and 3D atmospheres, the latter are required to adequately reproduce MAVEN observations.
- The hot oxygen corona plays an important role in protecting the Martian ionosphere and thermosphere from the solar wind erosion.
- The thermospheric oxygen atom is the primary neutral source for O^+ ion escape during the relatively weak solar cycle 24.

Corresponding author: Chuanfei Dong, dcfy@princeton.edu

Abstract

We study roles of the thermosphere and exosphere on the Martian ionospheric structure and ion escape rates in the process of the solar wind-Mars interaction. We employ a four-species multifluid MHD (MF-MHD) model to simulate the Martian ionosphere and magnetosphere. The *cold* thermosphere background is taken from the Mars Global Ionosphere Thermosphere Model (M-GITM) and the hot oxygen exosphere is adopted from the Mars exosphere Monte Carlo model - Adaptive Mesh Particle Simulator (AMPS). A total of four cases with the combination of 1D (globally averaged) and 3D thermospheres and exospheres are studied.

The ion escape rates calculated by adopting 1D and 3D atmospheres are similar; however, the latter are required to adequately reproduce MAVEN ionospheric observations. In addition, our simulations show that the 3D hot oxygen corona plays an important role in preventing planetary molecular ions (O_2^+ and CO_2^+) escaping from Mars, mainly resulting from the mass loading of the high-altitude exospheric O^+ ions. The *cold* thermospheric oxygen atom, however, is demonstrated to be the primary neutral source for O^+ ion escape during the relatively weak solar cycle 24.

1 Introduction

Unlike Earth and Venus, Mars with a relatively weak surface gravity allows an extended corona of hot oxygen that can partially escape to space [*Wallis*, 1978; *Ip*, 1988; *Nagy and Cravens*, 1988; *Fox*, 1993]. Being the most important reaction, the dissociative recombination of O_2^+ (deep in the dayside thermosphere/ionosphere) is responsible for producing most of dayside exospheric hot atomic oxygen ($O_2^+ + e \longrightarrow O^* + O^*$), therefore, the distribution of the hot oxygen exosphere is asymmetric around the Mars globe [*Valeille et al.*, 2009; *Lee et al.*, 2015a]. Note that it is not only the model that shows the hot O distribution is asymmetric, but it is also seen in the MAVEN Imaging Ultraviolet Spectrograph (IUVS) data [e.g., *Lee et al.*, 2015b; *Leblanc et al.*, 2017]. In addition to the dissociative recombination of O_2^+, the sputtering caused by collisions between the pickup ions (e.g., O^+) and the Martian thermospheric background may also be an important source for the hot corona [*Luhmann and Kozyra*, 1991; *Johnson and Luhmann*, 1998; *Leblanc et al.*, 2018]. Compared with the *cold* thermospheric background, the *hot* (or energetic) oxygen has a thermal speed, $\langle v_O \rangle = (2k_B T_O/m_O)^{\frac{1}{2}}$, higher than the local thermal speed of the thermosphere.

Besides the strong day-night asymmetry exhibited in the hot oxygen density distribution, the major neutral species in the Martian thermosphere (CO_2 and O) are also distributed asymmetrically about the planet [e.g., *Bougher et al.*, 2008; *Bougher et al.*, 2015a]. Specifically, more neutral CO_2 molecules are in the dayside thermosphere than on the nightside at a given altitude because the CO_2 global distribution is mainly controlled by the global temperature instead of the dynamics. Therefore, the thermospheric CO_2 density increases (decreases) on the dayside (nightside) where temperatures are higher (lower). The density distribution of atomic O (especially on the nightside), however, is mainly controlled by the day-night transport due to its relatively low mass; photochemistry may make certain contribution on the dayside oxygen density distribution. For atomic O, transport begins to have an effect as the thermospheric winds increase with increasing altitude above the region where dayside O is produced photochemically; the day-to-night atomic O distribution is impacted strongly by winds roughly above ~130 km [*Bougher et al.*, 2015a]. The neutral wind can transport atomic O from dayside to nightside, resulting in a bulge of neutral O in the nightside thermosphere [*Bougher et al.*, 2015a].

In order to capture the asymmetry in the Martian thermosphere and exosphere, three-dimensional "whole atmosphere" (from the ground to the exobase, 0 to ~ 250 km) [*Bougher et al.*, 2015a] and exosphere [*Lee et al.*, 2015a] models are ultimately required to capture these asymmetric features. The modeled thermosphere and exosphere can be further input

into a global plasma code as the neutral background, such that roles of the 3D thermosphere and exosphere on the Martian ionospheric structure and ion escape processes can be investigated in detail. Note that the incident solar wind at Mars encounters an extended hot exosphere, a conductive ionosphere, and highly localized crustal magnetic fields (the strongest of which in the southern hemisphere [*Acuña et al.*, 1999]), resulting in a complex obstacle to the solar wind that varies on all spatial and temporal scales. Among all the objects in the solar system, Mars, therefore, offers a uniquely challenging set of conditions to simulate.

In recent years, investigations of the Martian thermosphere/ionosphere structure [e.g., *Withers et al.*, 2015; *Bougher et al.*, 2015b], magnetic topology [e.g., *Luhmann et al.*, 2015; *Xu et al.*, 2016; *Liemohn et al.*, 2017; *DiBraccio et al.*, 2018], and atmospheric ion escape rates [e.g., *Halekas et al.*, 2016; *Fang et al.*, 2017; *Egan et al.*, 2018] have become increasingly important because they are closely related to the evolution of the Martian atmosphere and can affect its climate over the past four billion years [e.g., *Jakosky et al.*, 2015a; *Bougher et al.*, 2015c; *Lillis et al.*, 2015, and the references therein]. In-situ spacecraft measurements [e.g., *Lundin et al.*, 2013; *Ramstad et al.*, 2015; *Dong et al.*, 2015c; *Brain et al.*, 2015] have greatly improved our estimates of global ion loss rates at the current epoch. By using Mars Express (MEX) Analyzer of Space Plasmas and Energetic Atoms 3 (ASPERA-3) data from June 2007 to January 2013, *Lundin et al.* [2013] reported that the average heavy ion escape rate increased approximately by a factor of 10, from 1×10^{24} s^{-1} (solar minimum) to 1×10^{25} s^{-1} (solar maximum). More recently, *Brain et al.* [2015] analyzed four months of Mars Atmosphere and Volatile EvolutioN (MAVEN) spacecraft data and estimated a net ion escape rate of $\sim 2.5 \times 10^{24}$ s^{-1} by choosing a spherical shell at ~1000 km above the planet with energies >25 eV during solar cycle maximum conditions. In addition, *Liemohn et al.* [2014] and *Dong et al.* [2015c] confirmed the substantial plume-like distribution of escaping ions from the Martian atmosphere in MEX and MAVEN observations, organized by the upstream solar wind convection electric field. It is also worth noting that the total ion loss rate increased by more than one order of magnitude during an interplanetary corona mass ejection (ICME) event observed by MAVEN on March 8th, 2015 [*Jakosky et al.*, 2015b; *Dong et al.*, 2015b; *Curry et al.*, 2015b; *Ma et al.*, 2017; *Luhmann et al.*, 2017]. Moreover, *Lingam et al.* [2018] found that the solar energetic protons (SEPs) associated with extreme space weather events with energies $\gtrsim$ 150 MeV can reach the Martian surface; the same cutoff value has also been presented by the Mars Science Laboratory's Curiosity rover group [*Hassler et al.*, 2014].

In order to study the solar wind interaction with the Martian upper atmosphere, various plasma fluid models and kinetic particle codes have been developed. A few notable examples include the multi-species single-fluid MHD models [*Ma et al.*, 2004, 2014], the multifluid MHD models [*Harnett and Winglee*, 2006; *Najib et al.*, 2011; *Riousset et al.*, 2013, 2014; *Dong et al.*, 2014a, 2015a], the test-particle approach [*Fang et al.*, 2008, 2010a; *Curry et al.*, 2014, 2015a] and the hybrid particle-in-cell (hybrid-PIC) codes [*Modolo et al.*, 2016; *Brecht et al.*, 2016]. These codes have been used to help quantify the ion escape rates from the Martian upper atmosphere through the solar wind-Mars interaction. Most of these studies can reach a reasonable agreement with the spacecraft observations. However, until now no systematic study was focused on the influence of 3D thermospheres and exospheres on the Martian ionospheric structure and ion escape rates.

In this paper, we adopt the 3D Mars thermosphere (i.e., neutral temperatures T_n, neutral densities n_O, n_{CO_2}, and photoionization frequencies I_O, I_{CO_2}) from the Mars Global Ionosphere Thermosphere Model (M-GITM) [*Bougher et al.*, 2015a] and the hot atomic oxygen density, $n_{O_{hot}}$, from the Mars exosphere Monte Carlo model - Adaptive Mesh Particle Simulator (AMPS) [*Lee et al.*, 2015a]. M-GITM and Mars AMPS are one-way coupled with the 3D Block-Adaptive-Tree-Solarwind-Roe-Upwind-Scheme (BATS-R-US) Mars multifluid MHD (MF-MHD) model [*Najib et al.*, 2011; *Dong et al.*, 2014a, 2015a] (see Figure 1 for the one-way coupled framework). The Mars AMPS hot oxygen corona

is calculated based on the thermosphere/ionosphere background from M-GITM [*Lee et al.*, 2015a]. In the present work, the simulations are carried out for four selected cases with the combination of 1D and 3D neutral atmospheres.

The remainder of this paper is divided into three sections. In Section 2, we briefly introduce the three models employed in this study. In Section 3.1, we investigate the role of the 3D thermosphere on the Martian ionospheric structure and ion escape rates by means of data-model and model-model comparisons. In Section 3.2, we study the effect of the 3D exosphere on the ion escape rate and the corresponding molecular to atomic escaping ion ratio $(O_2^+ + CO_2^+)/O^+$ through model-model comparisons. Discussion and Conclusions are summarized in the last section.

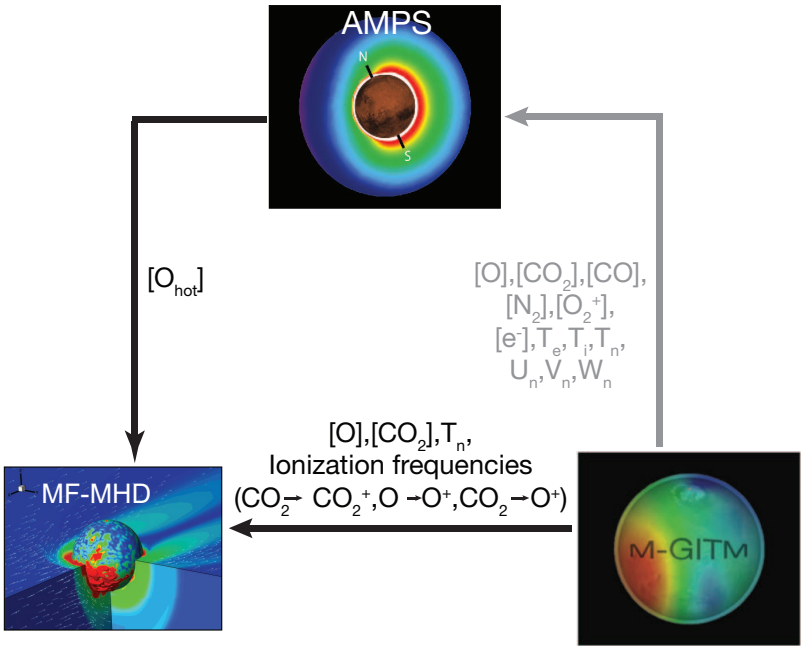

Figure 1. Sketch of a one-way coupling approach between M-GITM, Mars AMPS and MF-MHD (after Figure 1 of *Dong et al.* [2015a]). The notation T_n denotes the neutral atmospheric temperature. The quantities [O], [CO_2], and [O_{hot}] are the thermospheric *cold* O, CO_2 and exospheric *hot* O number densities, respectively. In this study, we adopt the one-way coupling indicated by the solid black lines. For the detailed study of the one-way coupling between M-GITM and Mars AMPS (solid gray line), please refer to *Lee et al.* [2015a].

2 Model Description

In this section, M-GITM, AMPS, and MF-MHD are briefly introduced. All these models have been adopted to support the MAVEN mission activities (2014-2018).

2.1 Mars Global Ionosphere Thermosphere Model (M-GITM)

Mars Global Ionosphere Thermosphere Model (M-GITM) [*Bougher et al.*, 2015a], combines the terrestrial GITM framework [*Ridley et al.*, 2006; *Deng et al.*, 2008] with the fundamental physical parameters, ion-neutral chemistry, and key radiative processes for Mars in order to capture the basic observed features of the thermal, compositional, and dynamical structure of the Mars atmosphere from the ground to the exobase (0 – 250

km). M-GITM currently solves for three-dimensional neutral and ion densities, as well as neutral temperatures and winds around the globe. Key neutral species presently include: CO_2, CO, O, N_2, O_2, Ar, and He. Five key photochemical ion species currently include: O^+, O_2^+, CO_2^+, N_2^+ and NO^+. Typically, production runs are conducted for a 5×5 degree longitude-latitude grid, with a constant 2.5 km vertical resolution (~ 0.25 scale height, $H_s = k_B T/mg$, where k_B is Boltzmann constant, g is the acceleration due to planetary gravity, T is the neutral temperature, and m is the mass of the neutral species).

M-GITM validation studies thus far have focused upon simulations for a range of solar cycles and seasonal conditions [*Bougher et al.*, 2015a,b, 2017]. Figure 2a shows the solar zenith angle (SZA) distribution around Mars' globe for aphelion solar moderate conditions (APHMOD) in the Geographic (GEO) coordinate system. The subsolar point (i.e., where SZA=0) is located in the northern hemisphere. An inspection of Figure 2b reveals that solar-driven exobase temperatures peak in the middle afternoon at the subsolar latitude (25°N). The warmer temperature near the evening terminator (LT = 18) is a result of the dynamical heating due to the convergent zonal winds [*Bougher et al.*, 2015a]. The asymmetric distribution of CO_2 in latitude (Figure 2c) is closely related to the asymmetric diurnal temperature distribution (Figure 2b). Conversely, Figure 2d presents atomic oxygen density distributions for which dayside-produced O is transported to the nightside by the thermospheric wind system, where it subsequently accumulates at low-to-middle latitudes around LT = 4–8. All the features shown in Figure 2 indicate the importance of adopting the 3D M-GITM thermosphere in a global plasma model in order to reproduce the ionospheric structure and accurately estimate the ion escape rates in the process of the solar wind-Mars interaction.

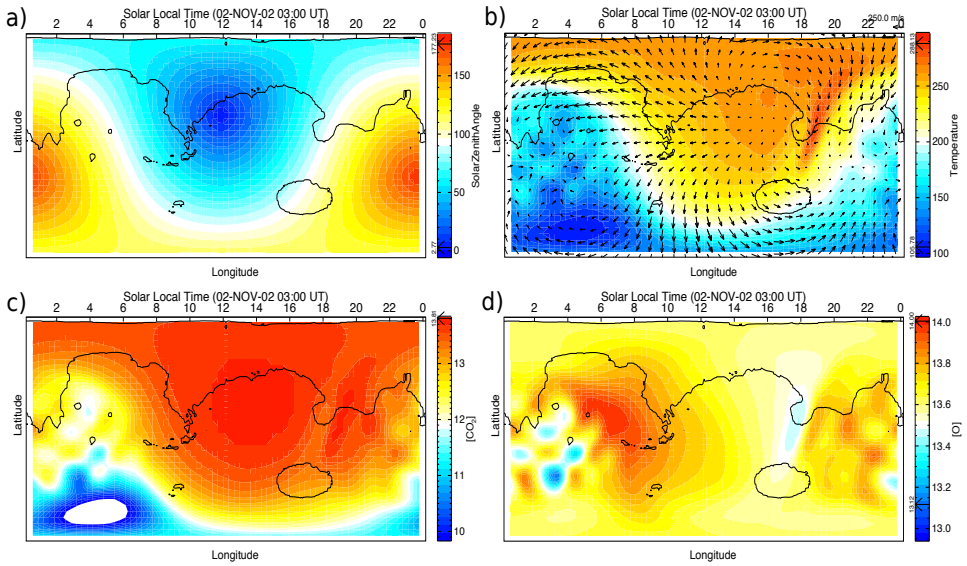

Figure 2. The color contours of (a) solar zenith angle (SZA, in degree), (b) Temperature (in K), (c) log10 CO_2 densities (in m^{-3}), and (d) log10 atomic O densities (in m^{-3}) at ~ 200 km (exobase) altitude for aphelion solar moderate conditions (APHMOD, Ls=90, $F_{10.7}$=130). The arrows in Figure 2 (b) indicate the relative magnitude and the direction of the horizontal winds. All the vertical axes (i.e., latitude) range from −90° to 90°. The white color highlights the regions below the low saturation of the colorbar.

2.2 Mars Adaptive Mesh Particle Simulator (AMPS)

The code we employ to model the Martian exosphere is the 3D Mars Adaptive Mesh Particle Simulator (AMPS), which runs in the test-particle mode using the Direct Simulation Monte Carlo (DSMC) method [*Bird*, 1994]. The AMPS code [*Tenishev and Combi*, 2008; *Tenishev et al.*, 2013a; *Lee et al.*, 2015a] is a well-tested code for a wide range of kinetic problems in rarefied gas regime. Examples of the AMPS applications include the cometary coma and the exospheres of Mars, Mercury and the Moon. The 3D structure and photochemical loss of hot oxygen particles from Mars have been investigated by taking advantage of the one-way coupled framework between Mars AMPS and M-GITM [*Lee et al.*, 2015a,b]. As shown in Figure 1, AMPS calculates the hot atomic oxygen density distribution based on the thermospheric background (i.e., neutral species O, CO_2, N_2, CO) from M-GITM.

Compared with the previous version where it assumed idealized hard sphere collisions and only isotropic scattering in the center of mass frame [*Valeille et al.*, 2009], the current AMPS considers a more realistic description for the collisions between hot O and ambient species by adopting a forward scattering collision scheme with the angular differential scattering cross sections from *Kharchenko et al.* [2000]. The related integrated cross sections (in cm^2) are 1.2×10^{-14} for O-CO_2, 6.4×10^{-15} for O-O, and 1.8×10^{-14} for both O-N_2 and O-CO. The current AMPS (by adopting the forward scattering scheme) produces a more intensive (and closer to observed) hot oxygen corona than the previous case by adopting the isotropic scattering scheme, and thus enhances the corresponding photochemical escape rate [*Lee et al.*, 2015a]. However, there still exists certain discrepancy between MAVEN observations and AMPS predictions [*Lee et al.*, 2015a]; further improvement of model predications of hot oxygen corona is an ongoing MAVEN effort.

The motion of each hot particle is influenced by the gravitational field of the Mars and modified by collisions with the background thermospheric species. The collision in the code depends on the rate of change in the background densities (i.e., rate of change in collision frequency). Although the nominal cell size is about 60 km at the model lower boundary (at 100 km altitude above the Martian surface), the large grid size does not prevent AMPS from capturing the variation in the Martian ionosphere and thermosphere. In AMPS, each macro-particle is initialized based on the thermospheric background prescribed by M-GITM (stored in an additional data table) at its resolution. It is noteworthy that the hybrid-PIC codes [e.g., *Modolo et al.*, 2016; *Brecht et al.*, 2016] have similar grid resolution for studying the solar-wind Mars interaction. The AMPS computational domain extends to 6 Mars radius (one Mars radius, $R_M \sim 3396$ km).

Figure 3 illustrates the hot and total (the sum of thermal and hot components) atomic oxygen distribution around the Mars globe in a logarithmic scale. Figure 3 is based on the Mars-centered Solar Orbital (MSO) coordinate system, where the $+X$ axis points from Mars to the Sun, the $+Z$ axis is perpendicular to the Martian orbital plane and points northward, and the Y axis completes the right-hand system. The left panels correspond to the global hot and total O distribution of the 1D spherically symmetric case, i.e., by averaging over all the longitudes and latitudes from the 3D AMPS output, $\overline{n}(r) = \frac{\iint n(r,\theta,\phi)\sin\theta d\theta d\phi}{\iint \sin\theta d\theta d\phi}$. The right panels show the original 3D AMPS and M-GITM output. An inspection of the second row of Figure 3 reveals that the thermal atomic oxygen dominates over the hot component at relatively low altitudes (i.e., in the thermosphere), while the hot atomic oxygen is the dominant neutral species at relatively high altitudes (i.e., in the exosphere). Both panels are for the aphelion solar moderate conditions (APHMOD). The 3D AMPS hot oxygen corona shows a great day-night asymmetry which cannot be captured by a 1D spherically symmetric profile. The remarkable asymmetry shown in Figure 3 indicates the significance of adopting the 3D hot oxygen corona in a global plasma code for studying the Martian atmospheric ion loss.

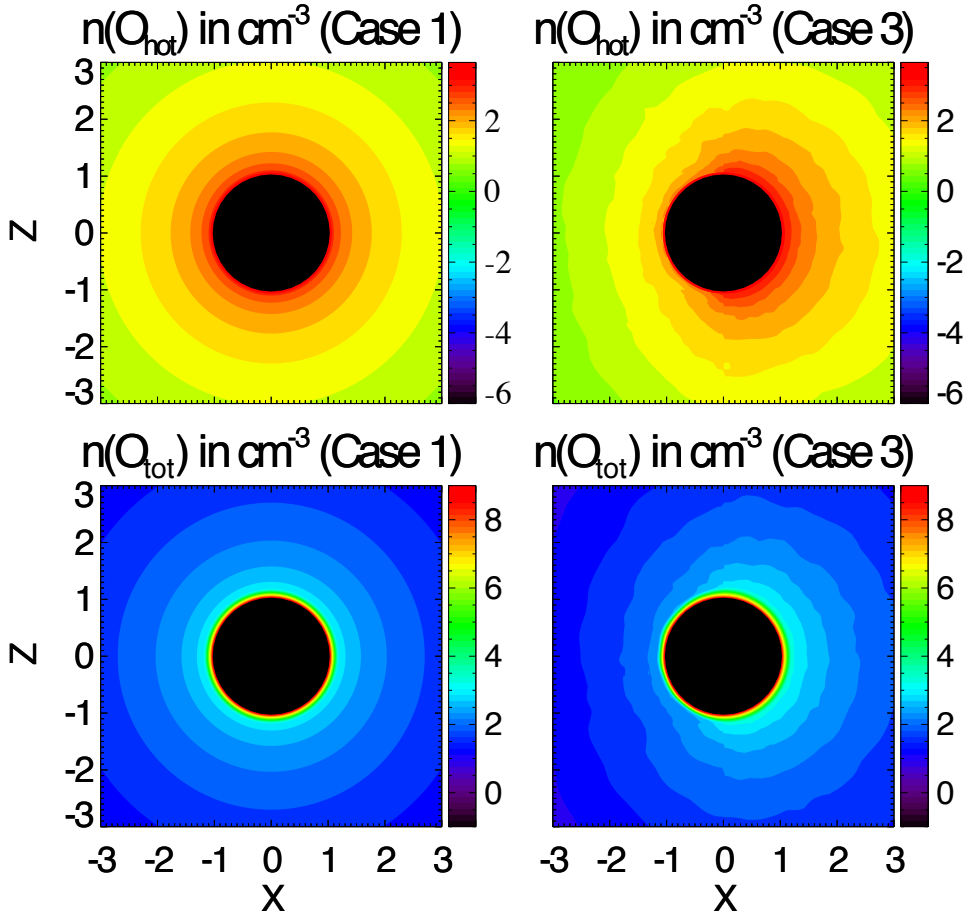

Figure 3. Comparisons of the hot atomic oxygen (first row) and total atomic oxygen (the sum of thermal and hot component, second row) density distribution (in cm^{-3}) from the globally averaged 1D spherically symmetric AMPS profile (left) and the 3D profile (right) in the x-z meridian plane in the MSO coordinate system. Both cases are based on the aphelion solar moderate conditions (APHMOD). Note the use of different logarithmic scales.

2.3 BATS-R-US Mars multifluid MHD (MF-MHD) Model

The 3D BATS-R-US multifluid MHD (MF-MHD) model solves separate continuity, momentum and energy equations for each fluid [*Powell et al.*, 1999; *Glocer et al.*, 2009; *Najib et al.*, 2011; *Tóth et al.*, 2012; *Huang et al.*, 2016; *Dong et al.*, 2017a]. For the Mars version, it solves MHD equations for four ion fluids H^+, O^+, O_2^+, CO_2^+ [*Najib et al.*, 2011; *Dong et al.*, 2014a, 2015a]. Interestingly, *Rubin et al.* [2014] showed that by using a multifluid MHD model, it can mimic some major features obtained with the hybrid-PIC calculation for a weak comet, such as the finite gyration effect of the planetary/cometary heavy ions and the associated pickup processes. The underlying reason is that MF-MHD includes the dynamics of individual ion species. The Lorentz force term, $\propto (\mathbf{u_s} - \mathbf{u_+}) \times \mathbf{B}$, in the individual ion momentum equation is mainly responsible for the asymmetric ion escape plume and the associated pickup processes, resulting from the difference between the charge averaged ion velocity, $\mathbf{u_+}$, and the individual fluid velocity, $\mathbf{u_s}$, of species s [*Dong et al.*, 2014a].

At the MF-MHD model lower boundary (100 km above the Martian surface), the densities of O^+, O_2^+, CO_2^+ satisfy the photochemical equilibrium condition [e.g. *Schunk*

Table 1. Chemical reactions and associated rates in Mars multifluid MHD code. The ion-neutral and ion-electron chemical reaction rates are adopted from *Najib et al.* [2011], while the photoionization frequencies (at the top of atmosphere for aphelion solar moderate conditions) are adopted from *Bougher et al.* [2015a] as indicated in Figure 1.

Chemical Reaction	Rate (s^{-1})
Primary Photolysis and Particle Impact	
$CO_2 + h\nu \rightarrow CO_2^+ + e^-$	8.37×10^{-7}
$CO_2 + h\nu \rightarrow CO + O^+ + e^-$	7.52×10^{-8}
$O + h\nu \rightarrow O^+ + e^-$	1.52×10^{-7}
$H + h\nu \rightarrow H^+ + e^-$	5.58×10^{-8}
$e^- + H \rightarrow e^- + H^+ + e^-$	see text
$e^- + O \rightarrow e^- + O^+ + e^-$	see text
Ion-Neutral Chemistry	Rate ($cm^3\ s^{-1}$)
$CO_2^+ + O \rightarrow O_2^+ + CO$	1.64×10^{-10}
$CO_2^+ + O \rightarrow O^+ + CO_2$	9.60×10^{-11}
$O^+ + CO_2 \rightarrow O_2^+ + CO$	$1.1 \times 10^{-9}\ (800/T_i)^{0.39}$
$O^+ + H \rightarrow H^+ + O$	6.4×10^{-10}
$H^+ + O \rightarrow O^+ + H$	5.08×10^{-10}
Ion-Electron Recombination Chemistry	Rate ($cm^3\ s^{-1}$)
$O_2^+ + e^- \rightarrow O + O$	$7.38 \times 10^{-8}\ (1200/T_e)^{0.56}$
$CO_2^+ + e^- \rightarrow CO + O$	$3.10 \times 10^{-7}\ (300/T_e)^{0.5}$

and Nagy, 2009, chapters 8 and 13]. A reflective inner boundary condition for the velocity **u** is used, which leads to an approximately zero velocity at the inner boundary as expected. The plasma temperature is set to be twice the value of the neutral temperature at the inner boundary, where both ions and electrons have roughly the same temperature as neutrals due to collisions. We use the 60 degree harmonic expansion model of *Arkani-Hamed* [2001] to describe the crustal magnetic fields at Mars [*Acuña et al.*, 1999]. The photochemical reactions in the model include charge exchange, photoionization, electron impact ionization and ion-electron recombination. The electron impact ionization rates are given by *Cravens et al.* [1987]. The elastic collision frequencies are taken from *Schunk and Nagy* [2009]. Table 1 summarizes the chemical reactions and the associated rates for inelastic collisions used in the multifluid MHD calculations.

The smallest radial resolution is about 5 km at the inner boundary while the grid size can increase to several thousand kilometers at the outer boundary ($\sim 30\ R_M$) due to the nonuniformity in the mesh design. The angular resolution varies from 1.5° to 3.0° in a spherical grid mesh bounded by a cube with $-30R_M \leq X \leq 8R_M$; $-30R_M \leq Y, Z \leq 30R_M$.

3 Simulation Results and Discussion

In this section, we discuss the simulation results obtained by using the one-way coupling approach, i.e., both the M-GITM and AMPS neutral profiles are used as the inputs for the MF-MHD model (Figure 1). Firstly, in order to study the effect of the 3D thermosphere on the Martian ionospheric structure and ion escape rates, we adopt either the 1D globally averaged (and thus spherically symmetric) thermosphere (Case 1) or the 3D M-

Table 2. Input parameters used for different cases. The solar cycle conditions are chosen based upon one MAVEN trajectory (orbit O2349) on 2015-12-14, during which it has a dayside periapsis.

Simulation #	Subsolar Position of Periapsis	Neutral Atmosphere	Solar Cycle Conditions
Case 1	167.9°E, 24.9°N	$1D_{cold}$ and $1D_{hot}$	Aphelion Solar
Case 2	167.9°E, 24.9°N	$3D_{cold}$ and $1D_{hot}$	Moderate
Case 3	167.9°E, 24.9°N	$3D_{cold}$ and $3D_{hot}$	(APHMOD)
Case 4	167.9°E, 24.9°N	$3D_{cold}$ without O_{hot}	

Table 3. Solar wind input parameters used for different cases. The solar wind inputs are taken from MAVEN measurements on 2015-12-14 (orbit O2349), during which it has a steady solar wind and IMF.

Simulation #	n_{sw} (cm^{-3})	v_{sw} (km/s)	IMF (nT)	T_{sw}^{proton} & $T_{sw}^{electron}$ (K)
Cases 1-4	4.85	(-348.5, -7.0, -25.5)	(-0.25, 5.5, -1.0)	5.9×10^4 & 1.3×10^5

Table 4. Calculated ion escape rates (in $\times10^{24}$ s^{-1}) and molecular to atomic escaping ion ratio listed in the last column.

Simulation cases	O^+	O_2^+	CO_2^+	Total	$(O_2^+ + CO_2^+)/O^+$
Case 1 ($1D_{cold}$ and $1D_{hot}$)	0.57	1.45	0.29	2.30	3.06
Case 2 ($3D_{cold}$ and $1D_{hot}$)	0.74	1.27	0.27	2.28	2.09
Case 3 ($3D_{cold}$ and $3D_{hot}$)	0.89	1.18	0.31	2.38	1.67
Case 4 ($3D_{cold}$ and noO_{hot})	0.88	1.52	0.40	2.80	2.17

GITM thermosphere (Case 2) while fixing the 1D globally averaged hot oxygen corona. Detailed data-model comparisons along a selected MAVEN trajectory on December 14, 2015 (orbit O2349) are studied. As an illustrative example, we also present the global ionospheric ion distribution at a constant altitude, 200 km, for both Cases 1 and 2. In Section 3.2, we investigate the role of the 3D exosphere on the ion escape rate. Three cases are studied for the aphelion solar moderate conditions (APHMOD) with a 1D corona, a 3D corona, and a case without a hot oxygen corona (Cases 2-4). Tables 2-3 summarize the parameters used for each case. The ion escape rates are summarized in Table 4.

3.1 Effects of 3D Thermosphere on the Solar Wind-Mars Interaction

We first focus on the effect of the 3D thermosphere on the solar wind-Mars interaction. Figure 4 presents the data-model comparison of the ionospheric density profiles between the MF-MHD calculations (dashed lines) and the MAVEN data (solid lines). The electron density was measured by the Langmuir Probe and Waves (LPW) instrument on board the spacecraft. The O^+, O_2^+ and CO_2^+ ion densities were measured by the Neutral Gas and Ion Mass Spectrometer (NGIMS). Figure 4a depicts the spacecraft altitudes (blue), latitude (black) and solar zenith angle (red) versus time along the trajectory. The rest of the panels are the detailed data-model comparisons based on the 1D thermosphere and exosphere (Case 1, Figure 4b), the 3D thermosphere and the 1D exosphere (Case 2, Figure 4c), and the 3D thermosphere and exosphere (Case 3, Figure 4d), respectively. In Figure 4, the MF-MHD model displays the maximum ionospheric ion and electron densities at the periapsis of orbit O2349 (on December 14, 2015), in good agreement with the MAVEN observation. Both the MF-MHD calculations and the MAVEN data reveal that O_2^+ is the dominant ion in the Martian ionosphere.

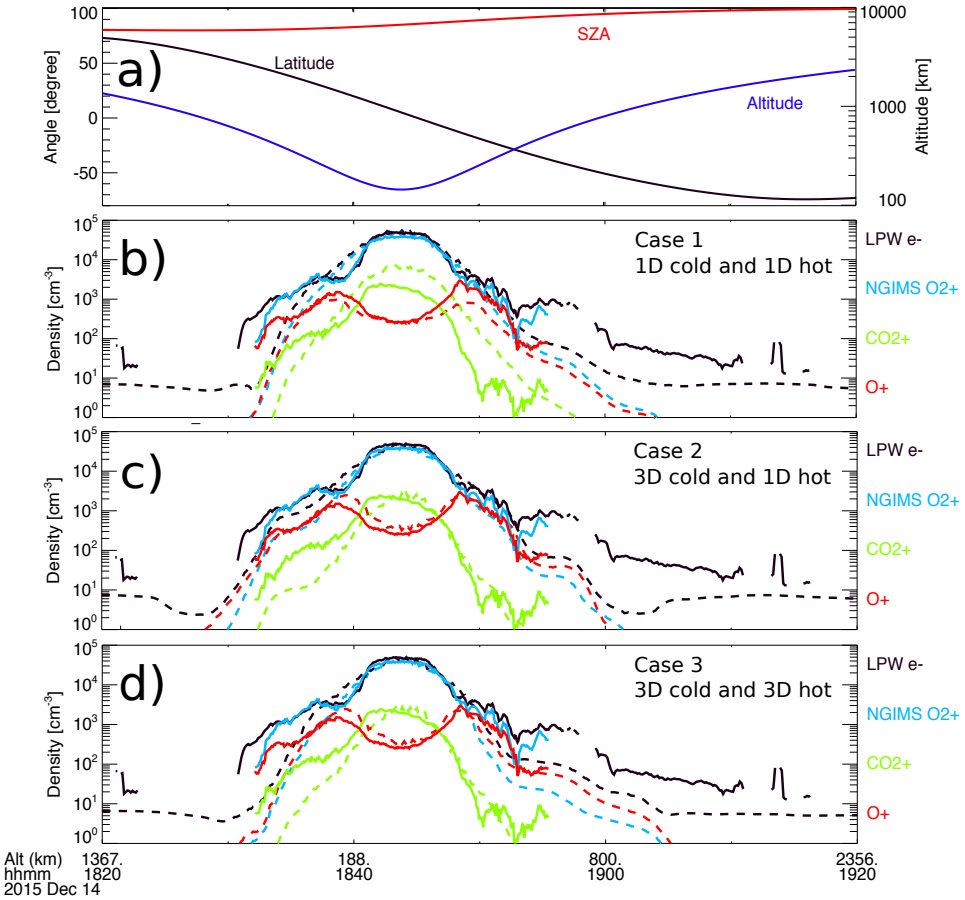

Figure 4. Comparisons of the ion and electron densities between the MF-MHD simulations (dashed lines) and the MAVEN observations (solid lines). The ion and electron densities are measured by NGIMS and LPW, respectively. Second panel: Case 1 with 1D thermosphere and exosphere. Third panel: Case 2 with 3D thermosphere and 1D exosphere. Fourth panel: Case 3 with 3D thermosphere and exosphere.

Compared with Case 1, the MF-MHD calculations based on the 3D M-GITM thermosphere (Case 2) fit the observational data better, demonstrating the importance of adopting the 3D thermosphere in a global plasma code. In Figure 4b, the calculated molecular ion (O_2^+ and CO_2^+) densities along the MAVEN trajectory are slightly higher than the NGIMS data whilst the O^+ ion density is slightly lower than that observed. Figure 4c, however, shows an opposite trend as presented in Figure 4b. In order to understand the deviation between simulations and observations, we plot both 1D and 3D thermospheric O and CO_2 densities along the MAVEN trajectory (Figure 5). As we expected, the 3D thermosphere (Case 2) has a higher O and lower CO_2 abundance compared to the 1D thermosphere (Case 1) along the MAVEN trajectory. This helps to explain the variation trend in the ion densities from Figure 4b to Figure 4c. An inspection of Figure 4c and Figure 4d reveals that the 3D hot oxygen does not have a significant effect on the ionospheric density distribution compared to the 1D exosphere case.

Although we have presented the ionospheric ion densities along one MAVEN trajectory, it is also important to depict the global density distribution of the Martian ionosphere. Figures 6 illustrates the 2D (latitude *vs.* local time, at 200-km altitude) ionospheric maps from the MF-MHD model for Case 1 (left column) and Case 2 (right column). For both cases, the top panels show the density distribution of O^+, and the middle

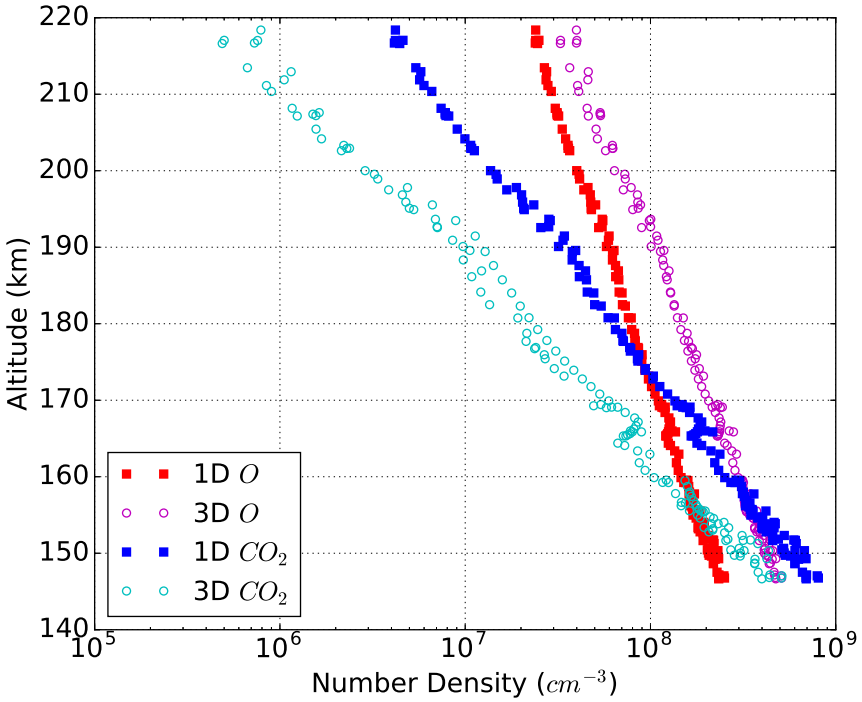

Figure 5. Comparisons between the 1D and 3D thermospheric density profiles along the MAVEN trajectory. The plot includes both inbound and outbound data.

to bottom panels display the density distribution of O_2^+ and CO_2^+, respectively. The smooth transition of the ion density around terminator region is a result of the implementation of Chapman function from *Smith and Smith* [1972] in the MF-MHD model. Again, both columns show that O_2^+ is the dominant ion species in the Martian ionosphere. In order to better understand the different ion distributions shown in Figure 4, we also plotted the projection of the MAVEN trajectory in each panel.

In Figure 6 (left column), all the ions mirror a similar ionospheric pattern as a result of the 1D spherically symmetric thermospheric input. The enhanced ion density in the southern hemisphere is mainly caused by the crustal magnetic fields given that the crustal anomalies are shifted to higher solar zenith angles (i.e. the southern polar region in MSO) at aphelion. The same enhancement at the southernmost latitudes seen in the left column is not present in the right column because the 3D asymmetric thermosphere (as shown in Figure 2) produces relatively high ion abundance at lower latitudes and northern hemisphere compared to the 1D thermosphere case. In Figure 6 (right column), however, the ionospheric global distributions between molecular ions (O_2^+ and CO_2^+) and atomic ions (O^+) are distinct when adopting the 3D thermosphere. On the other hand, O_2^+ and CO_2^+ share similar ionospheric patterns. It is well known that the Martian dayside ionosphere is triggered by the photoionization resulting from the solar EUV radiation [*Bougher et al.*, 2008]. Subsequently, the photoionized CO_2^+ quickly reacts with neutral O to produce the major ionospheric species O_2^+; therefore, O_2^+ exhibits a similar ionospheric distribution as CO_2^+. The ionospheric density peaks of O_2^+ and CO_2^+ are also located at almost the identical altitude (e.g., see Figure 7). Although thermospheric O can be photoionized by photons (the main channel), ionized through charge exchange with other ion species, and impact ionized by electrons to produce O^+, the absence of the neutral oxygen atom (in the

dayside thermosphere in 3D case) leads to a low abundance of O^+ in the dayside ionosphere (right column of Figures 6), consistent with the neutral density distribution shown in Figure 2. Compared with the previous work, O^+ in the present work can also be produced through photoionization of CO_2 as a secondary channel.

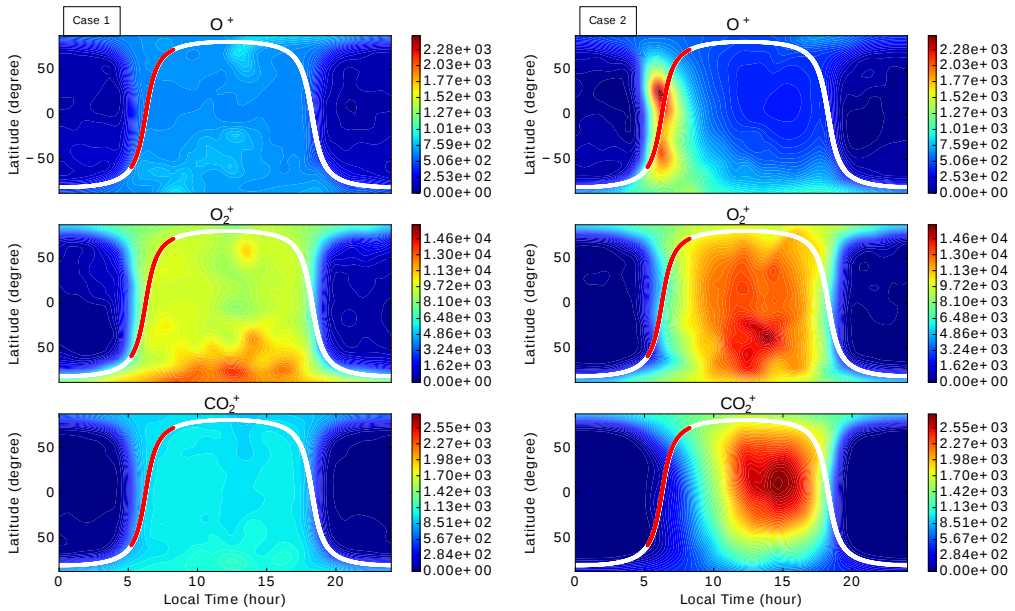

Figure 6. The ionospheric density maps for O^+, O_2^+, and CO_2^+ at 200-km altitude for Case 1 (left column) and Case 2 (right column). The thick white curve in each panel represents the projection of a selected MAVEN trajectory (orbit O2349 on December 14, 2015). The red segment corresponds to the regions with altitudes lower than 1000 km, including the periapsis. Note the use of different colorbar range in different rows.

In order to understand the effect of the 3D thermosphere on the ion escape, we calculate the ion escape rates and list them in Table 4. The calculations are conducted by integrals of the plasma density multiplied by the radial velocity component at the surface of a sphere far from the planet. Calculations (not presented here for the sake of brevity) show that ion escape rates do not change to any significant degree (<~5%) once the radius exceeds 5 R_M, the result presented in the remainder of this paper use the integral sphere with radius 6 R_M. Compared with Case 1 (with 1D globally averaged thermosphere), the O^+ ion escape rate in Case 2 (with 3D thermosphere) increases whilst molecular ionospheric ion (O_2^+ and CO_2^+) escape rate deceases. These trends can be explained by the vertical ionospheric density profiles (at SZA=0) shown in Figure 7. As seen from Figure 7, more O^+ at lower altitudes for Case 1 and more molecular ionospheric ions (O_2^+ and CO_2^+) at lower altitudes for Case 2, consistent with Figure 6. The relative abundance, however, shows a contrary trend at high altitudes (in the yellow shading region). Interestingly, the high-altitude ion abundance is consistent with the ion escape rates listed in Table 4 since only those ions above a certain altitude (i.e., ion exobase) are able to escape [e.g., *Cravens et al.*, 2017]. From test-particle simulations, *Fang et al.* [2010b] also found that generally on the dayside, only less than 35% of ions are able to escape below 400-km altitude.

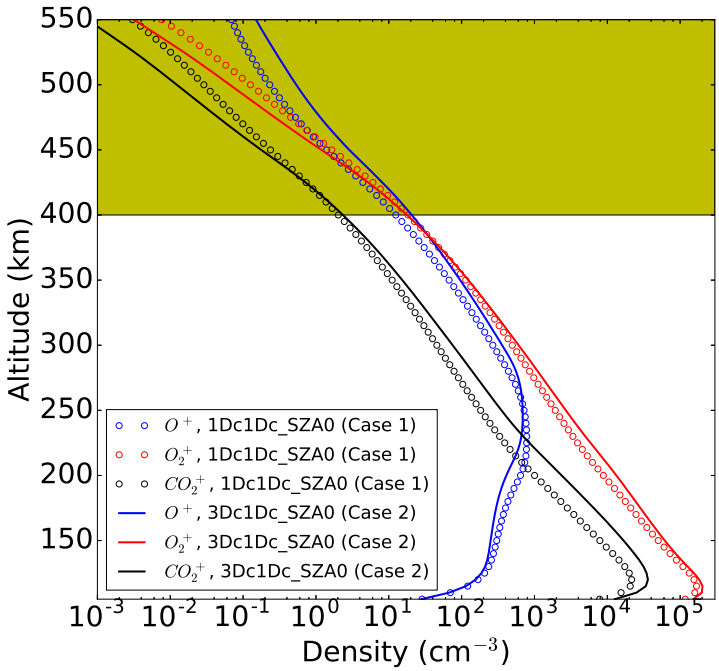

Figure 7. The vertical ionospheric density profiles for O^+, O_2^+, and CO_2^+ at SZA=0 for Case 1 (circle markers) and Case 2 (solid curves). The yellow shading highlights a region that is more relevant to the ion escape.

3.2 Effects of 3D Exosphere on the Solar Wind-Mars Interaction

In order to investigate the effect of the 3D exosphere (i.e., hot oxygen corona) on the interplay between the Martian upper atmosphere and the solar wind, we study three cases with a 1D corona, a 3D corona, and a case without a hot oxygen corona (Cases 2-4). This is similar to the study by *Curry et al.* [2013b], who conducted test-particle simulations to study O^+ ion loss rates with and without the 1D hot oxygen corona from *Kim et al.* [1998] by fixing the 1D thermosphere from *Ma et al.* [2004].

3.2.1 Effects of 3D Hot Oxygen Corona on O^+ Ion Escape

Figure 8 depicts the O^+ density in the x-z plane. One of the features of the MF-MHD model is that it can capture the asymmetric escape plume of the planetary pickup ions [*Najib et al.*, 2011; *Dong et al.*, 2014a; *Rubin et al.*, 2014]. Both Cases 2 and 3 present dayside pickup O^+ ion escaping from the extended hot oxygen corona region whilst the high-altitude corona O^+ ions cannot be observed in Case 4 due to the absence of an atomic oxygen source. Compared with Case 2, more O^+ are present in the dayside exospheric region in Case 3, consistent with those hot oxygen density distributions shown in Figure 9. All three cases present a large number of O^+ ions escaping from the nightside plasma wake region as well. The color contours in Figure 8 can be used to explain why the O^+ ion escape rate of Case 2 is smallest among three cases and O^+ ion escape rates between Case 3 and Case 4 are similar. The similar ion escape rate between Case 3 and Case 4 implies that the thermospheric oxygen atoms make a significant contribution on the O^+ ion escape rate.

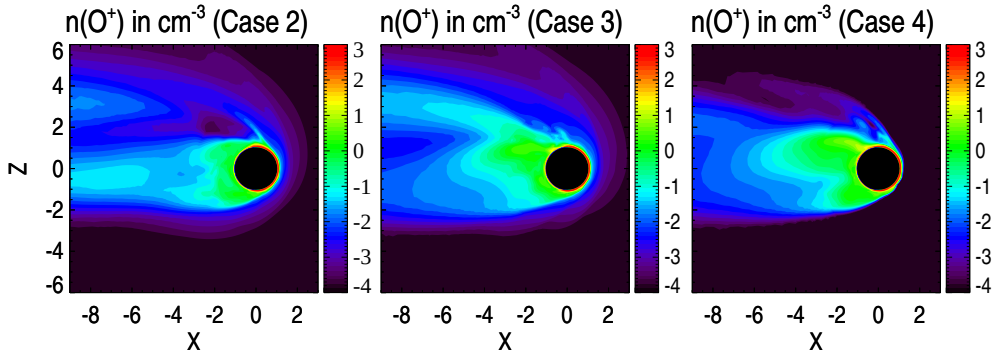

Figure 8. Comparisons of O^+ density in the x-z plane for a 1D corona, a 3D corona, and a case without a hot oxygen corona. Left: case with the 1D globally averaged hot oxygen corona (Case 2). Middle: case with the 3D AMPS hot oxygen corona (Case 3). Right: case without the hot oxygen corona (Case 4). Note the use of a logarithmic scale.

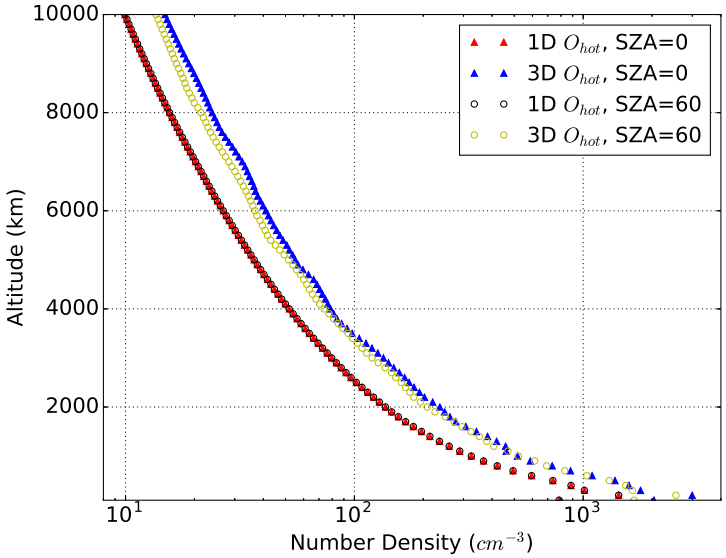

Figure 9. The comparison between 1D and 3D exospheric hot oxygen profiles at SZA=0 and SZA=60.

3.2.2 Effects of 3D Hot Oxygen Corona on Ion Escape: O^+ vs. *(O_2^+ and CO_2^+)*

In this section, we will focus on Cases 3-4 and aim to understand the effect of a 3D hot oxygen on O^+ ion escape versus ionospheric molecular ion (O_2^+ and CO_2^+) losses. We summarize the calculated ion escape rates for Cases 3-4 in Table 4.

Compared with Case 3 that includes hot oxygen, Case 4 (without hot oxygen) has higher O_2^+ and CO_2^+ escape rates but maintains a similar value of O^+ escape rate. The variation in the molecular to atomic escaping ion ratio (i.e., the last column of Table 4) indicates that the hot oxygen component has a shielding effect that can protect the Martian ionosphere from the solar wind erosion, especially for O_2^+ and CO_2^+ that have a relatively high mass and thus are located at relatively low altitudes. It also reveals that the thermo-

spheric oxygen is the dominant neutral source in determining the Martian O^+ ion escape for APHMOD under the nominal solar wind conditions.

Before proceeding further, recall that *Dong et al.* [2015a] calculated the ion escape rates under different solar cycle and seasonal conditions. They found that O_2^+ is the dominant escaping ion at solar minimum whilst O^+ is the dominant escaping species at solar maximum. *Curry et al.* [2013a] also showed the importance of O^+ ion escape using a test-particle model at solar maximum. Therefore, we conduct a case study by choosing Case 10 (autumnal equinox solar maximum - AEQUMAX) in *Dong et al.* [2015a] with and without 3D hot oxygen corona; the O^+ ion escape rates are 4.57×10^{24} s^{-1} and 3.70×10^{24} s^{-1}, respectively. Compared with APHMOD, the hot oxygen becomes more important for O^+ ion escape at AEQUMAX. The thermospheric oxygen atom, however, is still the primary neutral source for O^+ ion escape for AEQUMAX under the nominal solar wind conditions.

The keys to understand the shielding effect of the hot oxygen corona are the ion pickup and mass loading processes. Given the momentum and energy conservation, the solar wind momentum and energy fluxes start to gradually decrease when approaching Mars due to the mass loading of high-altitude O^+ (ionized from hot oxygen corona). In the absence of a hot oxygen corona, the solar wind can directly interact with the Martian ionosphere and thermosphere.

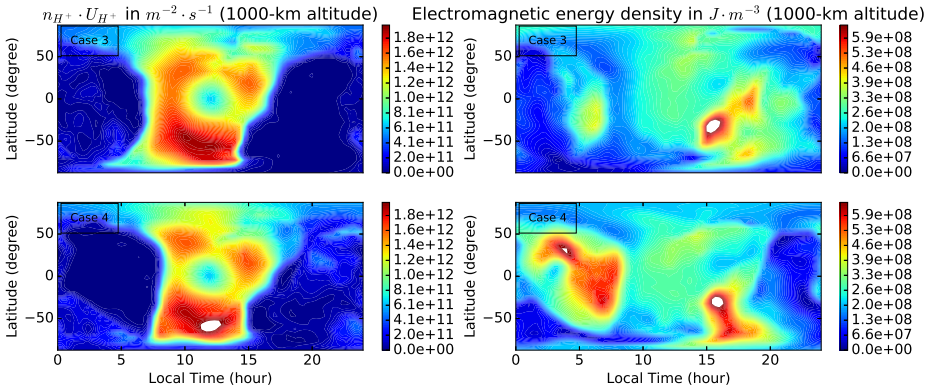

Figure 10. Comparisons of the solar wind proton number flux, $n_{H^+}U_{H^+}$ between Case 3 and Case 4 (left). Comparisons of the electromagnetic energy density, $\mathcal{E}$ between Case 3 and Case 4 (right). Both are depicted at 1000-km altitude above the Martian surface. The white color highlights the regions beyond the high saturation of the colorbar.

Figure 10 demonstrates the solar wind proton number flux (left) and the electromagnetic energy density (right) at 1000 km above the Martian surface for Cases 3 and 4. The electromagnetic energy density is defined as

$$\mathcal{E} = \frac{\epsilon_0 E^2}{2} + \frac{B^2}{2\mu_0} \tag{1}$$

where ϵ_0 and μ_0 are the permittivity and permeability of free space, respectively. E denotes the electric field (see Eq.(2) in *Dong et al.* [2014a]) and B represents the magnetic field. In Figure 10 (left panel), the proton number flux in Case 4 is saturated at 1000-km altitude (in white) while no saturation is observed in Case 3 using the same colorbar range. Compared with Case 4, less electromagnetic energy density (right panel of Figure

10) is available at same altitude in Case 3, indicating the ionosphere is more disturbed by the solar wind without a hot oxygen corona.

4 Conclusions

Recently, *Dong et al.* [2017b, 2018] studied the atmospheric ion escape of exoplanets (such as Proxima b and the TRAPPIST-1 system by assuming Venus-like atmospheres) orbiting M-dwarfs in the close-in habitable zone. Due to the strong EUV flux and extreme stellar wind parameters, they found that the O^+ ion is always the dominant escaping ion species (due to its relatively small mass and thus large scale height) compared to O_2^+ and CO_2^+. In certain circumstances, the ionospheric molecular ion (O_2^+ and CO_2^+) escape rates of Venus-like exoplanets orbiting M-dwarfs are similar to (and even smaller than) the cases in our solar system despite the much more intensive stellar radiation and stellar wind, as a result of the short star-planet distance, e.g, 0.05 AU for Proxima b. The underlying reason is that the mass loading of relatively light O^+ ion slows down the stellar wind. At ancient times, the EUV flux and solar wind parameters were much stronger than that of the current epoch (partly resembling those of the M-dwarf exoplanets discussed earlier), and Mars also has a much more extensive and intensive hot oxygen corona [*Valeille et al.*, 2010], indicating that hot oxygen exosphere may provide an important source for O^+ ion escaping billions of years ago. Therefore, the hot oxygen corona may play a crucial role in the long-term evolution of the Martian atmosphere and its composition over its history [*Dong et al.*, 2014b]. Based on this study, we speculate that the early loss rate of the ionospheric molecular ions (O_2^+ and CO_2^+) may be even lower than the current value due to the strong shielding (i.e., mass loading) effect of high-altitude oxygen ions.

In summary, we studied the solar wind interaction with the Martian upper atmosphere using a one-way coupled framework of three comprehensive 3D models, i.e., the M-GITM thermosphere output and the Mars AMPS hot atomic oxygen corona are used as the inputs for the MF-MHD model. The effects of 1D and 3D *cold* thermosphere and *hot* oxygen corona on the ionospheric structure and ion escape rates are studied in detail by comparing four selected cases. While the total ion escape rates by adopting 1D and 3D neutral atmospheres are similar, the detailed ionospheric density distributions are distinguishable. Compared with the 1D thermosphere, the MF-MHD calculations based on 3D thermosphere are in better agreement with MAVEN observations. We also found that the hot oxygen corona plays an important role in protecting the Martian ionosphere and thermosphere from the solar wind erosion, i.e., reducing the molecular ionospheric ion (O_2^+ and CO_2^+) escape rate. The shielding effect can be explained by the mass loading of the high-altitude hot oxygen ions. Moreover, the simulation results reveal that the *cold* oxygen is the primary neutral source for O^+ ion escape during this unusually quiet solar cycle.

Acknowledgments

The authors thank M. Lingam for the helpful discussions and comments. This research was supported by NASA grant NNH10CC04C through MAVEN Project, managed by Laboratory for Atmospheric and Space Physics at the University of Colorado Boulder. It was also supported by NASA grants 80NSSC18K0288, NNX14AH19G and NNX16AQ04G. Resources supporting this work were provided by the NASA High-End Computing (HEC) Program through the NASA Advanced Supercomputing (NAS) Division at Ames Research Center. We also would like to acknowledge high-performance computing support from Yellowstone (ark:/85065/d7wd3xhc) and Cheyenne (doi:10.5065/D6RX99HX) provided by NCAR's Computational and Information Systems Laboratory, sponsored by the National Science Foundation. The Space Weather Modeling Framework that contains the BATS-R-US code used in this study is publicly available from `http://csem.engin.umich.edu/tools/swmf`. The MAVEN data is publicly available through the Planetary Plasma Interactions Node of

the Planetary Data System `https://pds-ppi.igpp.ucla.edu/mission/MAVEN`. The model results are publicly available at `https://umich.box.com/s/tas6l27xzupb4dvkp2whz7k6wklnwes3`.

References

Acuña, M. H. et al. (1999), Global Distribution of Crustal Magnetization Discovered by the Mars Global Surveyor MAG/ER Experiment, *Science*, *284*, 790–793, doi: 10.1126/science.279.5357.1676.

Arkani-Hamed, J. (2001), A 50-degree spherical harmonic model of the magnetic field of Mars, *Journal of Geophysical Research*, *106*, 23,197–23,208.

Bird, G. A., (1994), Molecular Gas Dynamics and the Direct Simulation of Gas Flows, 2nd ed., Clarendon Press, Oxford.

Bougher, S. W., P.-L. Blelly, M. R. Combi, J. L. Fox, I. Mueller-Wodarg, A. Ridley, and R. G. Roble (2008), Neutral Upper Atmosphere and Ionosphere Modeling, *Space Sci. Reviews*, *139*, 107-141, doi:10.1007/s11214-008-9401-9.

Bougher, S. W., D. J. Pawlowski, J. M. Bell, S. Nelli, T. McDunn, J. R. Murphy, M. Chizek, and A. Ridley (2015a), Mars global ionosphere-thermosphere model (MGITM): Solar cycle, seasonal, and diurnal variations of the Mars upper atmosphere, *Journal of Geophysical Research*, *120* 311–342, doi:10.1002/2014JE004715.

Bougher, S., et al. (2015b), Early MAVEN Deep Dip campaign reveals thermosphere and ionosphere variability, *Science*, *350*, 0459, doi:10.1126/science.aad0459.

Bougher, S. W., T. E. Cravens, J. Grebowsky, and J. Luhmann (2015c), The Aeronomy of Mars: Characterization by MAVEN of the Upper Atmosphere Reservoir that Regulates Volatile Escape, *Space Science Reviews*, *195*, 423–456, doi:10.1007/s11214-014-0053-7.

Bougher, S. W., K. Roeten, K. Olsen, P. R. Mahaffy, M. Benna, M. Elrod, S. Jain, N. M. Schneider, J. Deighan, E. Thiemann, F. G. Eparvier, A. Stiepen, and B. Jakosky (2017), The structure and variability of Mars dayside thermosphere from MAVEN NGIMS and IUVS measurements: Seasonal and solar activity trends in scale heights and temperatures, *Journal of Geophysical Research*, *122*, 1296–1313, doi:10.1002/2016JA023454.

Brain, D. A., J. P. McFadden, J. S. Halekas, J. E. P. Connerney, S. W. Bougher, S. Curry, C. F. Dong, Y. Dong, F. Eparvier, X. Fang, K. Fortier, T. Hara, Y. Harada, B. M. Jakosky, R. J. Lillis, R. Livi, J. G. Luhmann, Y. Ma, R. Modolo, and K. Seki (2015), The spatial distribution of planetary ion fluxes near Mars observed by MAVEN, *Geophys. Res. Lett.*, *42*, 9142–9148, doi:10.1002/2015GL065293.

Brecht, S. H., S. A. Ledvina and S. W. Bougher (2016), Ionospheric loss from Mars as predicted by hybrid particle simulations, *J. Geophys. Res. Space Physics*, *121*, 10,190–10,208.

Cravens, T. E., J. U. Kozyra, A. F. Nagy, T. I. Gombosi, and M. Kurtz (1987), Electron impact ionization in the vicinity of comets, *Journal of Geophysical Research*, *92*, 7341–7353.

Cravens, T. E., Hamil, O., Houston, S., Bougher, S., Ma, Y., Brain, D. and Ledvina, S. (2017), Estimates of ionospheric transport and ion loss at Mars, *Journal of Geophysical Research: Space Physics*, *122*, 10,626–10,637.

Curry, S. M., M. W. Liemohn, X.-H. Fang, Y.-J. Ma, J. Espley (2013a), The influence of production mechanisms on pick-up ion loss at Mars, *Journal of Geophysical Research*, *118*, 554–569, doi:10.1029/2012JA017665.

Curry, S. M., M. Liemohn, X. Fang, D. Brain, and Y. Ma (2013b), Simulated kinetic effects of the corona and solar cycle on high altitude ion transport at Mars, *Journal of Geophysical Research*, *118*, 3700–3711, doi:10.1002/jgra.50358.

Curry, S. M., M. W. Liemohn, X.-H. Fang, Y.-J. Ma, J. Slavin, J. Espley, S. Bougher, and C. F. Dong (2014), Test particle comparison of heavy atomic and molecular ion distributions at Mars, *Journal of Geophysical Research*, *119*, 2328–2344, doi: 10.1002/2013JA019221.

Curry, S. M., J. G. Luhmann, Y. Ma, M. W. Liemohn, C. Dong, and T. Hara (2015a), Comparative pick-up ion distributions at Mars and Venus: Consequences for atmospheric deposition and escape, *Planet. Space Sci.*, *115*, 35–47, doi: 10.1016/j.pss.2015.03.026.

Curry, S. M., J. G. Luhmann, Y. J. Ma, C. F. Dong, D. Brain, F. Leblanc, R. Modolo, Y. Dong, J. McFadden, J. Halekas, J.E.P. Connerney, J. Espley, T. Hara, Y. Harada, C. Lee, X. Fang, and B. Jakosky (2015b), Response of Mars O+ Pick-up Ions to the March 8th, 2015 ICME: Inferences from MAVEN Data-Based Models, *Geophys. Res. Lett.*, *42*, 9095–9102, doi:10.1002/2015GL065304.

Deng, Y., A. D. Richmond, A. J. Ridley, and H.-L. Liu (2008), Assessment of the non-hydrostatic effect on the upper atmosphere using a general circulation model (GCM), *Geophysical Research Letters*, *35*, L01104, doi:10.1029/2007GL032182

DiBraccio, G. A., J. G. Luhmann, S. M. Curry, J. R. Espley, S. Xu, D. L. Mitchell, Y. Ma, C. Dong, J. R. Gruesbeck, J. E. P. Connerney, Y. Harada, S. Ruhunusiri, J. S. Halekas, Y. Soobiah, T. Hara, D. A. Brain, B. M. Jakosky (2018), The Twisted Configuration of the Martian Magnetotail: MAVEN Observations, *Geophysical Research Letters*, doi: 10.1029/2018GL077251.

Dong, C., S. W. Bougher, Y. Ma, G. Toth, A. F. Nagy, and D. Najib (2014a), Solar wind interaction with Mars upper atmosphere: Results from the one-way coupling between the multifluid MHD model and the MTGCM model, *Geophysical Research Letters*, *41*, 2708–2715, doi:10.1002/2014GL059515.

Dong, C., S. W. Bougher, Y. Ma, G. Toth, Y. Lee, A. F. Nagy, V. Tenishev, D. Pawlowski and M. Combi (2014b), Solar Wind Interaction with the Martian Upper Atmosphere at Early Mars/Extreme Solar Conditions, *AGU Fall Meeting Abstracts*, abstract P53C-4032.

Dong, C., S. W. Bougher, Y. Ma, G. Toth, Y. Lee, A. F. Nagy, V. Tenishev, D. J. Pawlowski, M. R. Combi, and D. Najib (2015a), Solar wind interaction with the Martian upper atmosphere: Crustal field orientation, solar cycle and seasonal variations, *J. Geophys. Res. Space Physics*, *120*, 7857–7872, doi:10.1002/2015JA020990.

Dong, C., Y. Ma, S. W. Bougher, G. Toth, A. F. Nagy, J. S. Halekas, Y. Dong, S. M. Curry, J. G. Luhmann, D. Brain, J. E. P. Connerney, J. Espley, P. Mahaffy, M. Benna, J. P. McFadden, D. L. Mitchell, G. A. DiBraccio, R. J. Lillis, B. M. Jakosky, and J. M. Grebowsky (2015b), Multifluid MHD study of the solar wind interaction with Mars' upper atmosphere during the 2015 March 8th ICME event, *Geophysical Research Letters*, *42*, 9103–9112, doi:10.1002/2015GL065944.

Dong, C, Z. Huang, M. Lingam, G. Toth, T. Gombosi, and A. Bhattacharjee (2017a), The dehydration of water worlds via atmospheric losses, *ApJ Letters*, *847*, L4.

Dong, C., M. Lingam, Y. J. Ma, and O. Cohen (2017b), Is Proxima Centauri B habitable? A study of atmospheric loss, *ApJ Letters*, *837*, L26.

Dong, C., M. Jin, M. Lingam, V. S. Airapetian, Y. J. Ma, B. van der Holst (2018), Atmospheric escape from the TRAPPIST-1 planets and implications for habitability, *Proceedings of the National Academy of Sciences*, *115*, 260–265, doi:10.1073/pnas.1708010115.

Dong, Y., X. Fang, D. A. Brain, J. P. McFadden, J. S. Halekas, J. E. Connerney, S. M. Curry, Y. Harada, J. G. Luhmann, B. M. Jakosky (2015c), Strong plume fluxes at Mars observed by MAVEN: An important planetary ion escape channel, *Geophysical Research Letters*, *42*, 8942–8950, doi:10.1002/2015GL065346.

Egan, H., Y. Ma, C. Dong, R. Modolo, R. Jarvinen, S. Bougher, J. Halekas, D. Brain, J. McFadden, J. Connerney, D. Mitchell, B. Jakosky (2018), Comparison of Global Martian Plasma Models in the Context of MAVEN Observations, *J. Geophys. Res. Space Physics*, doi:10.1029/2017JA025068.

Fang, X., M. W. Liemohn, A. F. Nagy, Y. Ma, D. L. De Zeeuw, J. U. Kozyra, and T. H. Zurbuchen (2008), Pickup oxygen ion velocity space and spatial distribution around Mars, *J. Geophys. Res.*, *113*, A02210, doi:10.1029/ 2007JA012736.

Fang, X., M. W. Liemohn, A. F. Nagy, J. G. Luhmann, and Y. J. Ma (2010a), On the effect of the martian crustal magnetic field on atmospheric erosion, *Icarus*, *206*, 130–138,

doi:10.1016/j.icarus.2009.01.012.

Fang, X., M. W. Liemohn, A. F. Nagy, J. G. Luhmann, and Y. Ma (2010b), Escape probability of Martian atmospheric ions: Controlling effects of the electromagnetic fields, *J. Geophys. Res.*, *115*, A04308, doi:10.1029/2009JA014929.

Fang,X., Y. J. Ma, K. Masunaga, Y. X. Dong, D. Brain, J. Halekas, R. Lillis, B. Jakosky, J. Connerney, J. Grebowsky, and C. F. Dong (2017), A quantitative study of the Mars crustal magnetic field control of plasma boundary locations and atmospheric loss: MHD prediction and comparison with MAVEN observations, *J. Geophys. Res. Space Physics*, *122*, 4117–4137, doi:10.1002/2016JA023509.

Glocer, A., G. Tóth, Y. J. Ma, T. I. Gombosi, J. C. Zhang, and L. M. Kistler (2009), Multifluid Block-Adaptive-Tree Solar Wind Roe-Type Upwind Scheme: Magnetospheric composition and dynamics during geomagnetic storms–Initial results, *J. Geophys. Res.*, *114*, A12203, doi:10.1029/2009JA014418.

Halekas, J. S., D. A. Brain, S. Ruhunusiri, J. P. McFadden, D. L. Mitchell, C. Mazelle, J. E. P. Connerney, Y. Harada, T. Hara, J. R. Espley, G. A. DiBraccio, B. M. Jakosky (2016), Plasma clouds and snowplows: Bulk plasma escape from Mars observed by MAVEN, *Geophys. Res. Lett.*, *43*, 1426–1434, doi:10.1002/2016GL067752.

Hanson, W. B., S. Sanatini, and D. R. Zuccaro (1977), The Martian ionosphere as observed by the Viking retarding potential analyzer, *J. Geophys. Res.*, *82*, 4351–4363.

Harnett, E. M., and R. M. Winglee (2006), Three-dimensional multifluid simulations of ionospheric loss at Mars from nominal solar wind conditions to magnetic cloud events, *J. Geophys. Res.*, *111*, A09213, doi:10.1029/2006JA011724.

Hassler, D. M., C. Zeitlin, R. F. Wimmer-Schweingruber, et al. (2014), Mars' Surface Radiation Environment Measured with the Mars Science Laboratory's Curiosity Rover, *Science*, *343*, 1244797.

Huang, Z. G., G. Toth, T. I. Gombosi, X. Z. Jia, M. Rubin, N. Fougere, V. Tenishev, M. R. Combi, A. Bieler, K. C. Hansen, Y. S. Shou, K. Altwegg (2016), Four-fluid MHD simulations of the plasma and neutral gas environment of comet 67P/Churyumov-Gerasimenko near perihelion, *J. Geophys. Res.*, *121*, 4247–4268, doi:10.1002/2015JA022333.

Ip, W. H. (1988), On a hot oxygen corona of Mars, *Icarus*, *76*, 135.

Jakosky, B. M. et al. (2015a), The Mars Atmosphere and Volatile Evolution (MAVEN) Mission, *Space Science Reviews*, *195*, 3–48, doi:10.1007/s11214-015-0139-x.

Jakosky, B. M., et al. (2015b), MAVEN observations of the response of Mars to an interplanetary coronal mass ejection, *Science*, *350*, 0210, doi:10.1126/science.aad0210.

Johnson, R. E., J. G. Luhmann (1998), Sputter contribution to the atmospheric corona on Mars, *J. Geophys. Res.*, *103*, 3649-3653.

Kharchenko, V., A. Dalgarno, B. Zygelman, and J. H. Yee (2000), Energy transfer in collisions of oxygen atoms in the terrestrial atmosphere, *J. Geophys. Res.*, *103*, 24,899–24,906.

Kim, J., A. F. Nagy, J. L. Fox, and T. E. Cravens (1998), Solar cycle variability of hot oxygen atoms at Mars, *J. Geophys. Res.*, *103*, 29,339.

Leblanc, F., J. Y. Chaufray, R. Modolo, L. Leclercq, S. Curry, J. Luhmann, R. Lillis, T. Hara, J. McFadden, J. Halekas, N. Schneider, J. Deighan, P. R. Mahaffy, M. Benna, R. E. Johnson, F. Gonzalez-Galindo, F. Forget, M. A. Lopez-Valverde, F. G. Eparvier, B. Jakosky (2017), On the Origins of Mars' Exospheric Nonthermal Oxygen Component as Observed by MAVEN and Modeled by HELIOSARES, *J. Geophys. Res. Planets*, *122*, 2401-2428, doi:10.1002/2017JE005336.

Leblanc, F., A. Martinez, J. Y. Chaufray, R. Modolo, T. Hara, J. Luhmann, R. Lillis, S. Curry, J. McFadden, J. Halekas, B. Jakosky (2018), On Mars' Atmospheric Sputtering after MAVEN first Martian year of Measurements, *Geophysical Research Letters*, doi:10.1002/2018GL077199.

Lee, Y., M. R. Combi, V. Tenishev, S. W. Bougher, and R. J. Lillis (2015a), Hot oxygen corona at Mars and the photochemical escape of oxygen: Improved description of the

thermosphere, ionosphere, and exosphere, *Journal of Geophysical Research (Planets)*, *120*, 1880–1892, doi:10.1002/2015JE004890.

Lee, Y., M. R. Combi, V. Tenishev, S. W. Bougher, J. Deighan, N. M. Schneider, W. E. McClintock, B. M. Jakosky (2015b), A comparison of 3-D model predictions of Mars' oxygen corona with early MAVEN IUVS observations, *Geophysical Research Letters*, *42*, 9015–9022, doi:10.1002/2015GL065291.

Liemohn, M. W., B. C. Johnson, M. Franz, and S. Barabash (2014), Mars Express observations of high altitude planetary ion beams and their relation to the "energetic plume" loss channel, *J. Geophys. Res. Space Physics*, *119*, 9702-9713, doi: 10.1002/2014JA019994.

Liemohn, M. W., S. Xu, C. Dong, S. W. Bougher, B. C. Johnson, R. Ilie, and D. L. De Zeeuw (2017), Ionospheric control of the dawn-dusk asymmetry of the Mars magnetotail current sheet, *J. Geophys. Res. Space Physics*, *122*, 6397-6414, doi: 10.1002/2016JA023707.

Lillis, R. J., D. A. Brain, S. W. Bougher, F. Leblanc, J. G. Luhmann, B. M. Jakosky, R. Modolo, J. Fox, J. Deighan, X. Fang, Y. C. Wang, Y. Lee, C. Dong, Y. Ma, T. Cravens, L. Andersson, S. M. Curry, N. Schneider, M. Combi, I. Stewart, J. Clarke, J. Grebowsky, D. L. Mitchell, R. Yelle, A. F. Nagy, D. Baker, and R. P. Lin (2015), Characterizing Atmospheric Escape from Mars Today and Through Time, with MAVEN, *SSRv*, *195*, 357–422, doi:10.1007/s11214-015-0165-8.

Fox, J. L. (1993), On the escape of oxygen and hydrogen from Mars, *Geophys. Res. Lett.*, *20*, 1747–1750.

Lingam, M., C. F. Dong, X. H. Fang, B. M. Jakosky, A. Loeb (2018), The propitious role of solar energetic particles in the origin of life, *ApJ*, *853*, 10.

Luhmann, J. G., and J. U. Kozyra (1991), Dayside pickup oxygen ion precipitation at Venus and Mars: Spatial distributions, energy deposition and consequences, *J. Geophys. Res.*, *96(A4)*, 5457–5467, doi:10.1029/90JA01753.

Luhmann, J. G., C.F. Dong, Y.J. Ma, S.M. Curry, D. Mitchell, J. Espley, J. Connerney, J. Halekas, D.A. Brain, B.M. Jakosky, and C. Mazelle (2015), Implications of MAVEN Mars Near-Wake Measurements and Models, *Geophys. Res. Lett.*, *42*, 9087–9094, doi: 10.1002/2015GL066122.

Luhmann, J. G., C. F. Dong, Y. J. Ma, S. M. Curry, S. Xu, C. O. Lee, T. Hara, J. Halekas, Yan Li, J. R. Gruesbeck, J. Espley, D. A. Brain, C. T. Russell (2017), Martian Magnetic Storms, *J. Geophys. Res. Space Physics*, *122*, 6185–6209, doi:10.1002/2016JA023513 .

Lundin, R., S. Barabash, M. Holmström, H. Nilsson, Y. Futaana, R. Ramstad, M. Yamauchi, E. M. Dubinin, and M. Fraenz, (2013), Solar cycle effects on the ion escape from Mars, *Geophysical Research Letters*, *40*, 6028–6032, doi:10.1002/2013GL058154.

Ma, Y. J., A. F. Nagy, I. V. Sokolov, and K. C. Hansen (2004), Three-dimensional, multispecies, high spatial resolution MHD studies of the solar wind interaction with Mars, *J. Geophys. Res. Space Physics*, *109*, A07,211, doi:10.1029/2003JA010367.

Ma, Y. J., X. Fang, C. T. Russell, A. F. Nagy, G. Toth, J. G. Luhmann, D. A. Brain, and C. Dong (2014), Effects of crustal field rotation on the solar wind plasma interaction with Mars, *Geophysical Research Letters*, *41*, doi:10.1002/2014GL060785.

Ma, Y. J., C. T. Russell, X. Fang, C. F. Dong, A. F. Nagy, G. Toth, J. S. Halekas, J. E. P. Connerney, J. R. Espley, P. R. Mahaffy, M. Benna, J. McFadden, D. Mitchell, L. Andersson, and B. M. Jakosky (2017), Variations of the Martian plasma environment during the ICME passage on 8 March 2015 – A time-dependent MHD study , *J. Geophys. Res. Space Physics*, *41*, 1714–1730, doi:10.1002/2016JA023402.

Modolo, R., et al. (2016), Mars-solar wind interaction: LatHyS, an improved parallel 3-D multispecies hybrid model, *J. Geophys. Res. Space Physics*, *121*, 6378–6399, doi: 10.1002/2015JA022324.

Nagy, A. F., and T. E. Cravens (1988), Hot oxygen atoms in the upper atmosphere of Venus and Mars, *Geophys. Res. Lett.*, *15*, 433–435, doi:10.1029/GL015i005p00433.

Najib, D., A. F. Nagy, G. Tóth, and Y. J. Ma (2011), Three-dimensional, multifluid, high spatial resolution MHD model studies of the solar wind interaction with Mars, *Journal of Geophysical Research*, *116*, A05,204, doi:10.1029/2010JA016272.

Powell, K. G., P. L. Roe, T. J. Linde, T. I. Gombosi, and D. L. De Zeeuw (1999), A Solution-Adaptive Upwind Scheme for Ideal Magnetohydrodynamics, *J. Computational Phys.*, *154*, 284–309.

Ramstad, R., S. Barabash, Y. Futaana, H. Nilsson, X.-D. Wang, M. Holmström (2015), The Martian atmospheric ion escape rate dependence on solar wind and solar EUV conditions I: Seven years of Mars Express observations, *Journal of Geophysical Research*, doi:10.1002/2015JE004816.

Ridley, A., Y. Deng, and G. Toth (2006), The global ionosphere-thermosphere model, *J. Atmos. Sol-Terr. Phys.*, *68*, 839.

Riousset, J. A., C. S. Paty, R. J. Lillis, M. O. Fillingim, S. L. England, P. G. Withers, and J. P. M. Hale (2013), Three-dimensional multifluid modeling of atmospheric electrodynamics in Mars' dynamo region, *Journal of Geophysical Research*, *118*, 1–13, doi: 10.1002/jgra.50328.

Riousset, J. A., C. S. Paty, R. J. Lillis, M. O. Fillingim, S. L. England, P. G. Withers, and J. P. M. Hale (2014), Electrodynamics of the Martian dynamo region near magnetic cusps and loops, *Geophysical Research Letters*, *41*, 1119–1125, doi: 10.1002/2013GL059130.

Rubin, M., , et al. (2014), Plasma environment of a weak comet - Predictions for Comet 67P/Churyumov-Gerasimenko from multifluid-MHD and Hybrid models, *Icarus*, *242*, 38–49.

Schunk, R. W., and A. F. Nagy (2009), Ionospheres, 2nd ed., Cambridge Univ. Press, New York, pp102–109, chapter 8, pp 483.

Smith F. L., and C. Smith (1972), Numerical evaluation of Chapman's grazing incidence integral ch (X, X), *Journal of Geophysical Research*, *77*, 3592–3597, doi: 10.1029/JA077i019p03592.

Tenishev, V., and M. Combi (2008), A global kinetic model for cometary comae: The evolution of the coma of the Rosetta target comet Churyumov-Gerasimenko throughout the mission, *ApJ*, *685*, 659–677.

Tenishev, V., M. Rubin, O. J. Tucker, M. R. Combi, and M. Sarantos (2013a), Kinetic modeling of sodium in the lunar exosphere, *Icarus*, *226*, 1538–1549, doi: 10.1016/j.icarus.2013.08.021.

Tóth, G. et al. (2012), Adaptive Numerical Algorithms in Space Weather Modeling, *J. Computational Phys.*, *231*, 870–903, doi:10.1016/j.jcp.2011.02.006.

Valeille, A., V. Tenishev, S. W. Bougher, M. R. Combi, and A. F. Nagy (2009), Three-dimensional study of Mars upper thermosphere/ionosphere and hot oxygen corona: 1. General description and results at equinox for solar low conditions, *Journal of Geophysical Research*, *114*, E11005, doi:10.1029/2009JE003388

Valeille, A., S. W. Bougher, V. Tenishev, M. R. Combi, A. F. Nagy (2010), Water loss and evolution of the upper atmosphere and exosphere over martian history, *Icarus*, *206*, 28–39, doi10.1016/j.icarus.2009.04.036.

Wallis, M. K. (1978), Exospheric density and escape fluxes of atomic isotopes on Venus and Mars, *Planet. Space Sci.*, *26*, 949.

Withers, P., M. Vogt, M. Mayyasi, P. Mahaffy, M. Benna, M. Elrod, S. Bougher, C.F. Dong, J.-Y. Chaufray,Y.J. Ma, and B. Jakosky (2015), Comparison of model predictions for the composition of the ionosphere of Mars to MAVEN NGIMS data, *Geophys. Res. Lett.*, *42*, 8966–8976, doi:10.1002/2015GL065205.

Xu, S., D. Mitchell, M. W. Liemohn, C. F. Dong, S. Bougher, M. Fillingim, R. Lillis, J. McFadden, C. Mazelle, J. Connerney, and B. Jakosky (2016), Deep nightside photoelectron observations by MAVEN SWEA: implications for Martian northern-hemispheric magnetic topology and nightside ionosphere source, *Geophys. Res. Lett.*, *43*, 8876–8884, doi:10.1002/2016GL070527.

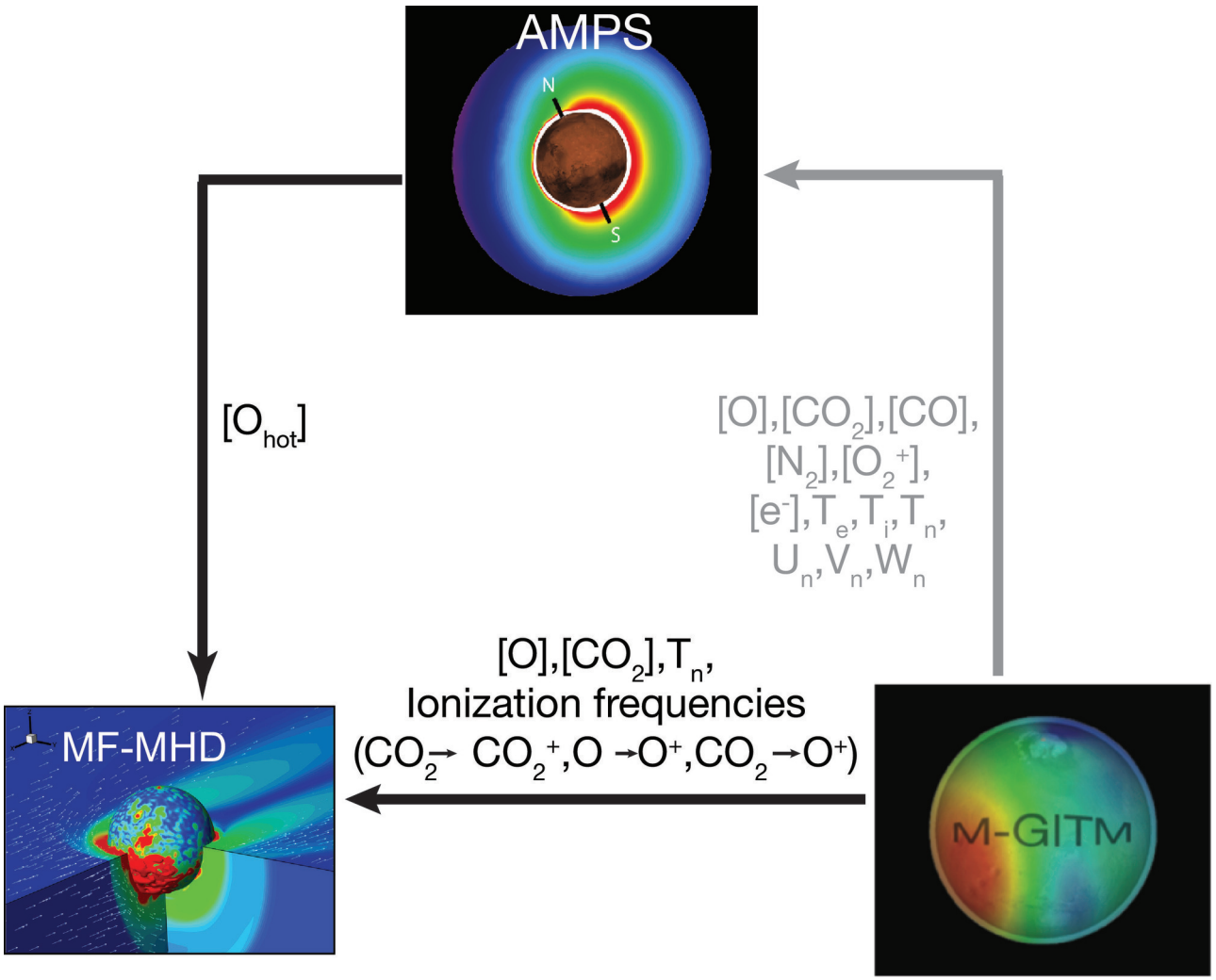

2018ja025543-f01-z-.eps

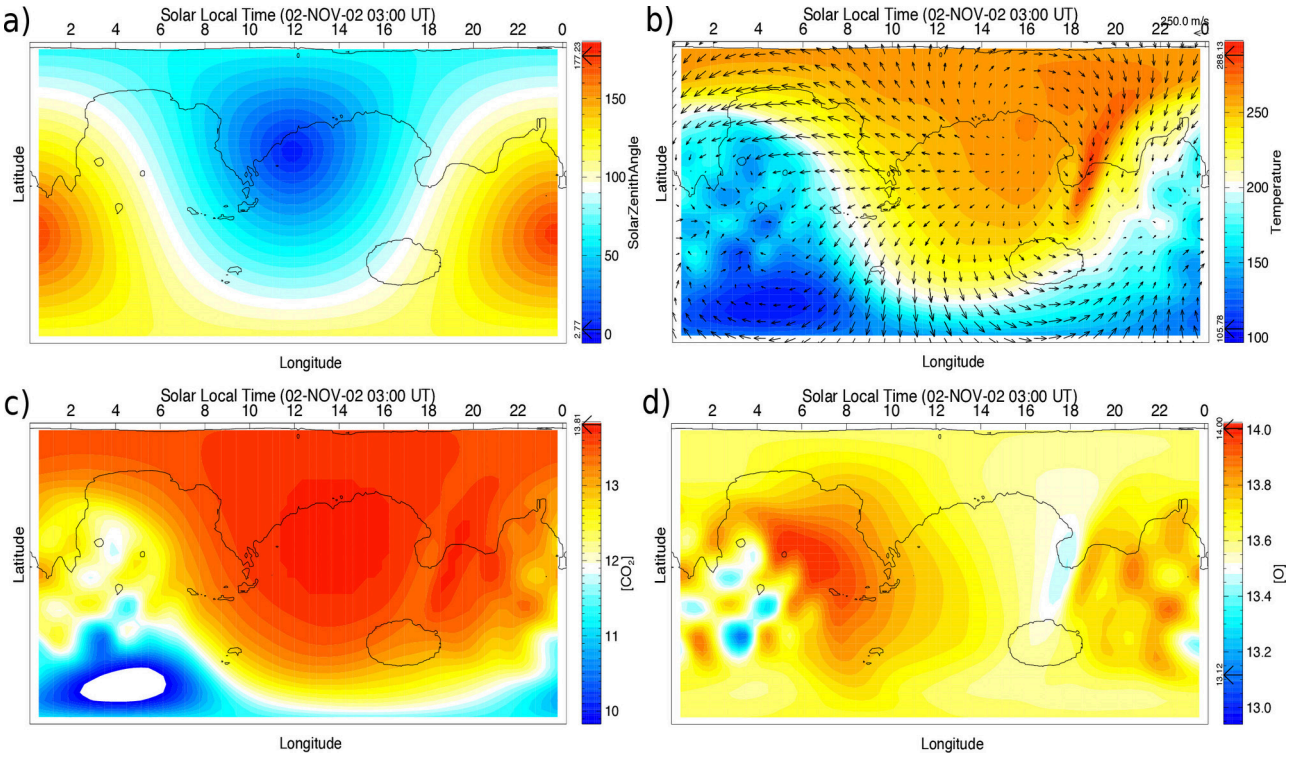

2018ja025543-f02-z-.eps

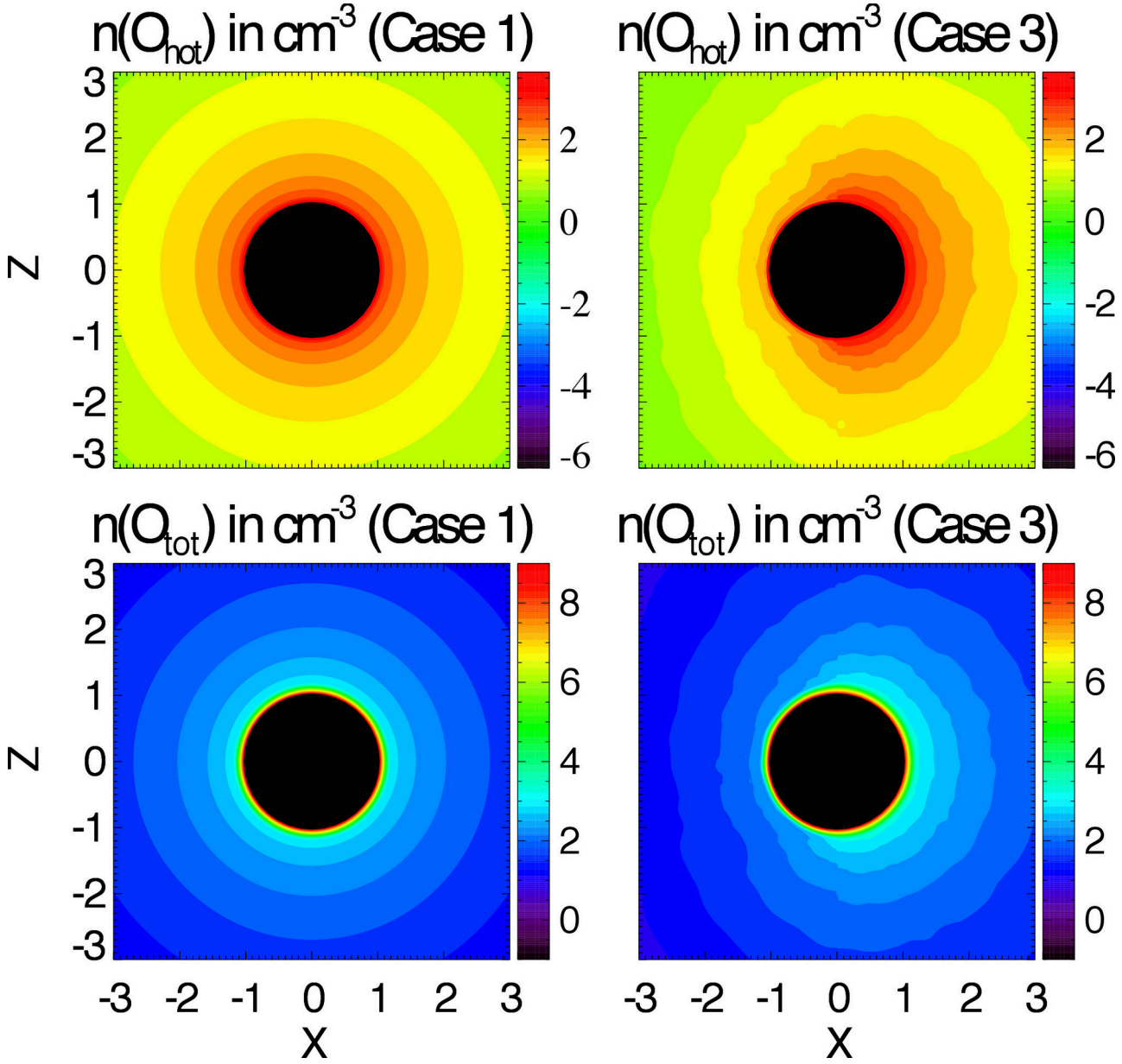

2018ja025543-f03-z-.eps

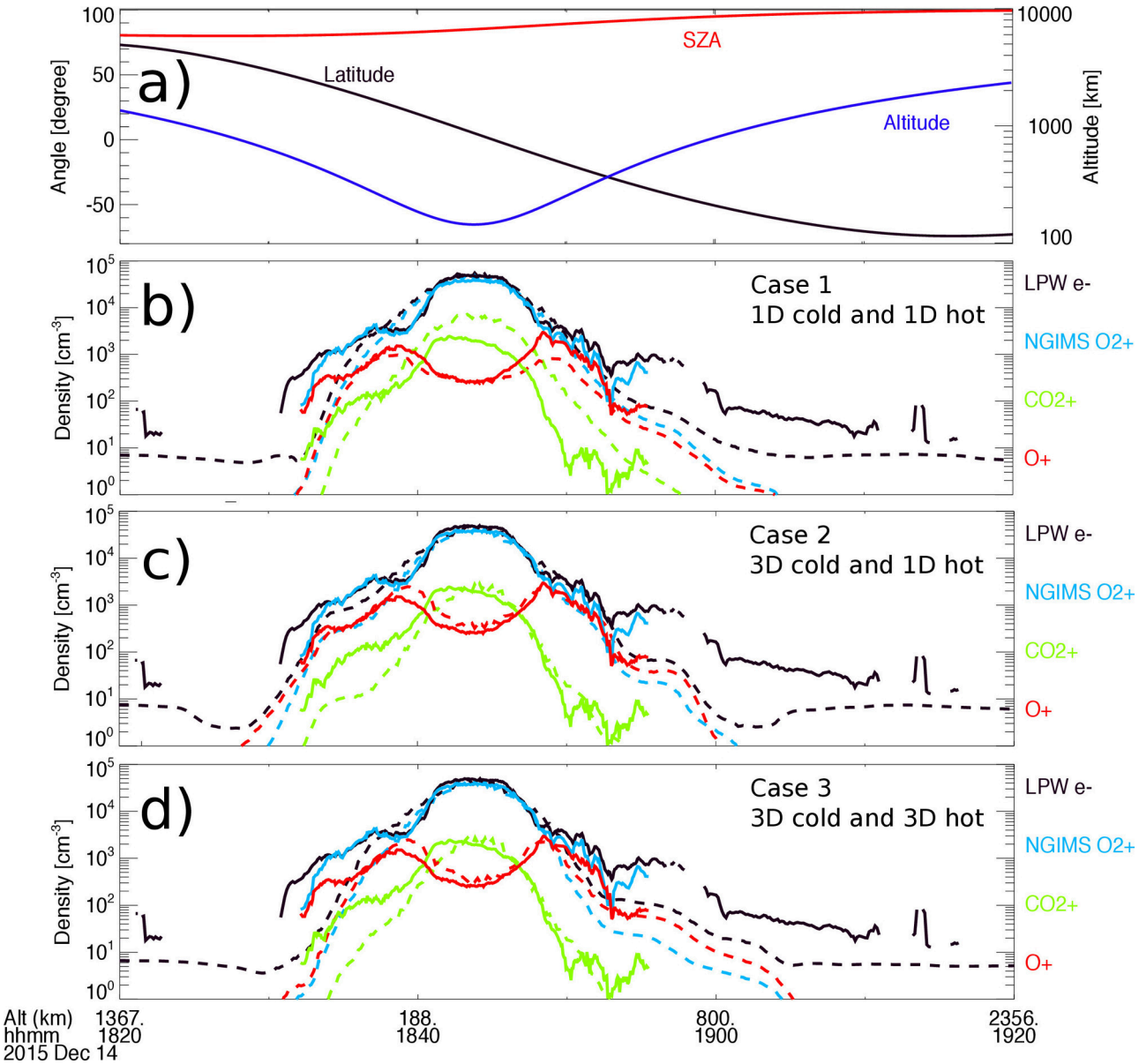

2018ja025543-f04-z-.eps

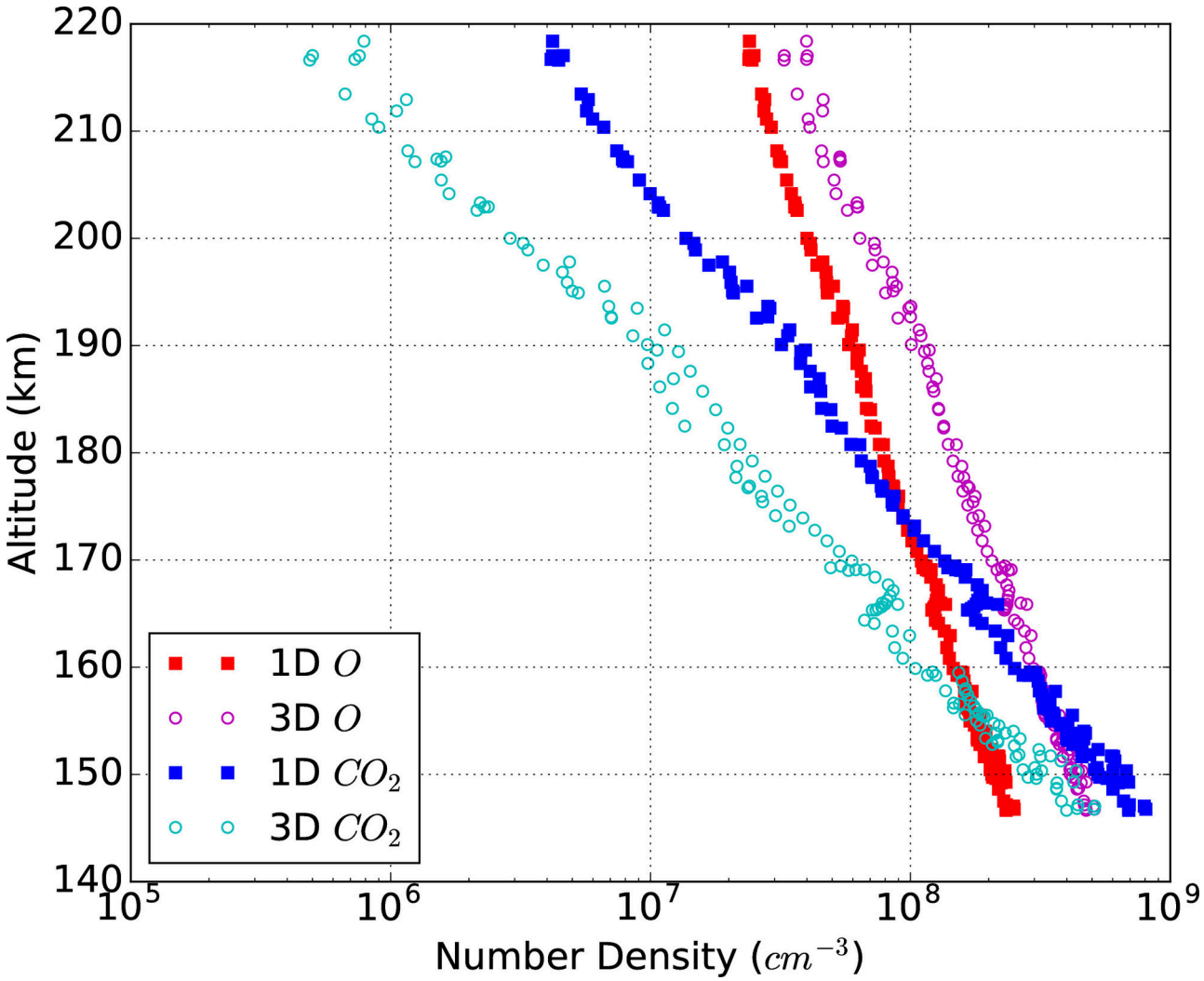

2018ja025543-f05-z-.eps

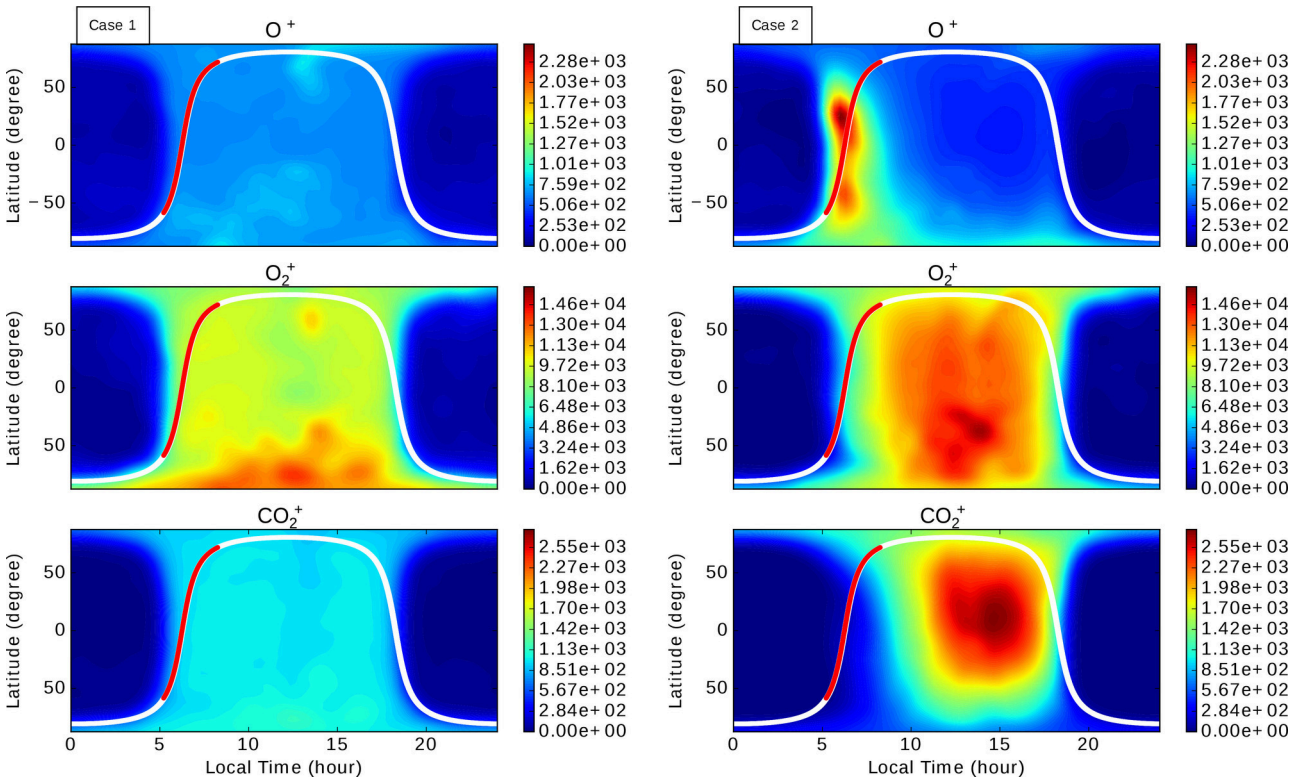

2018ja025543-f06-z-.eps

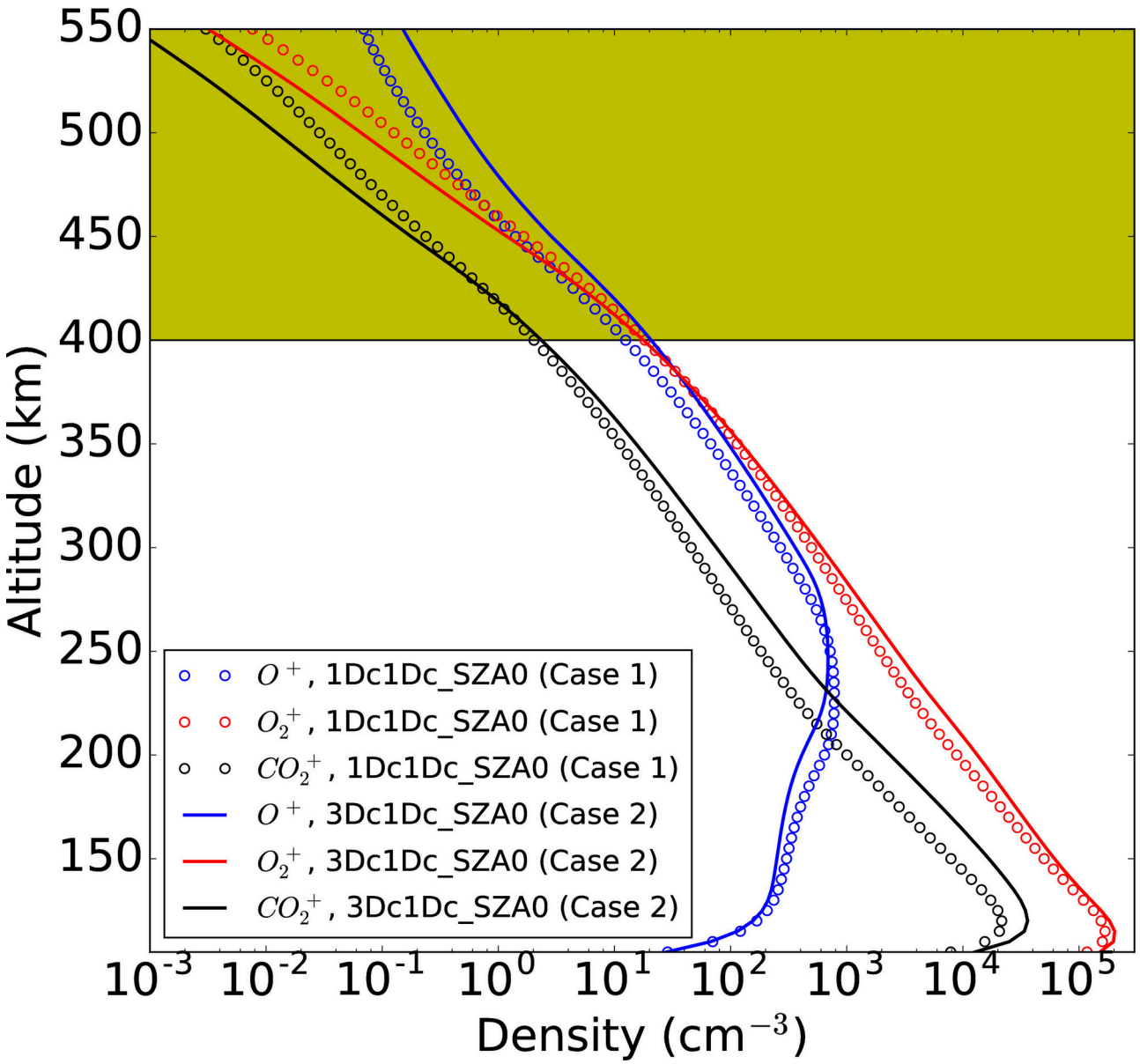

2018ja025543-f07-z-.eps

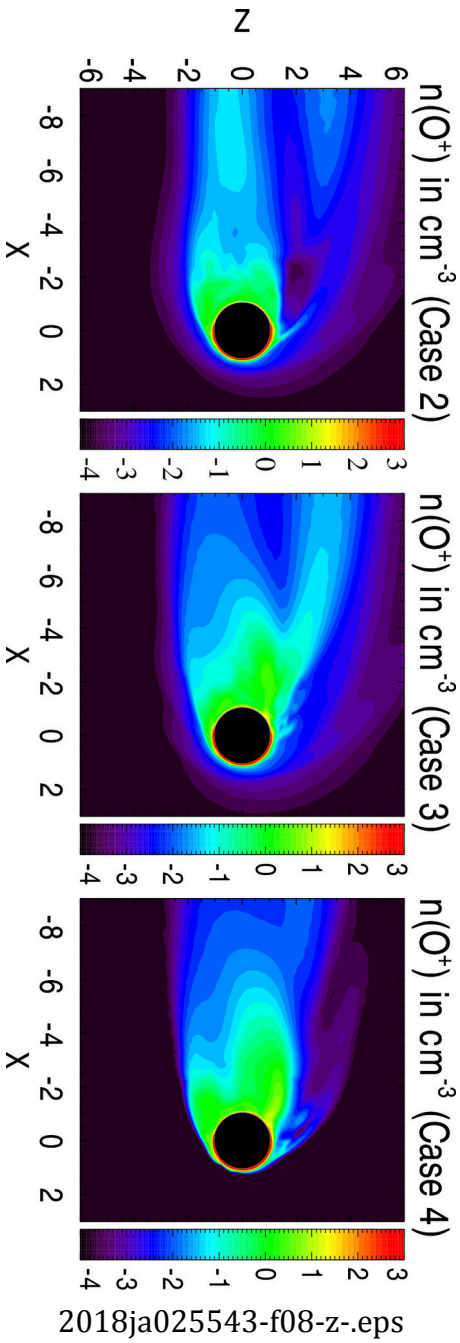

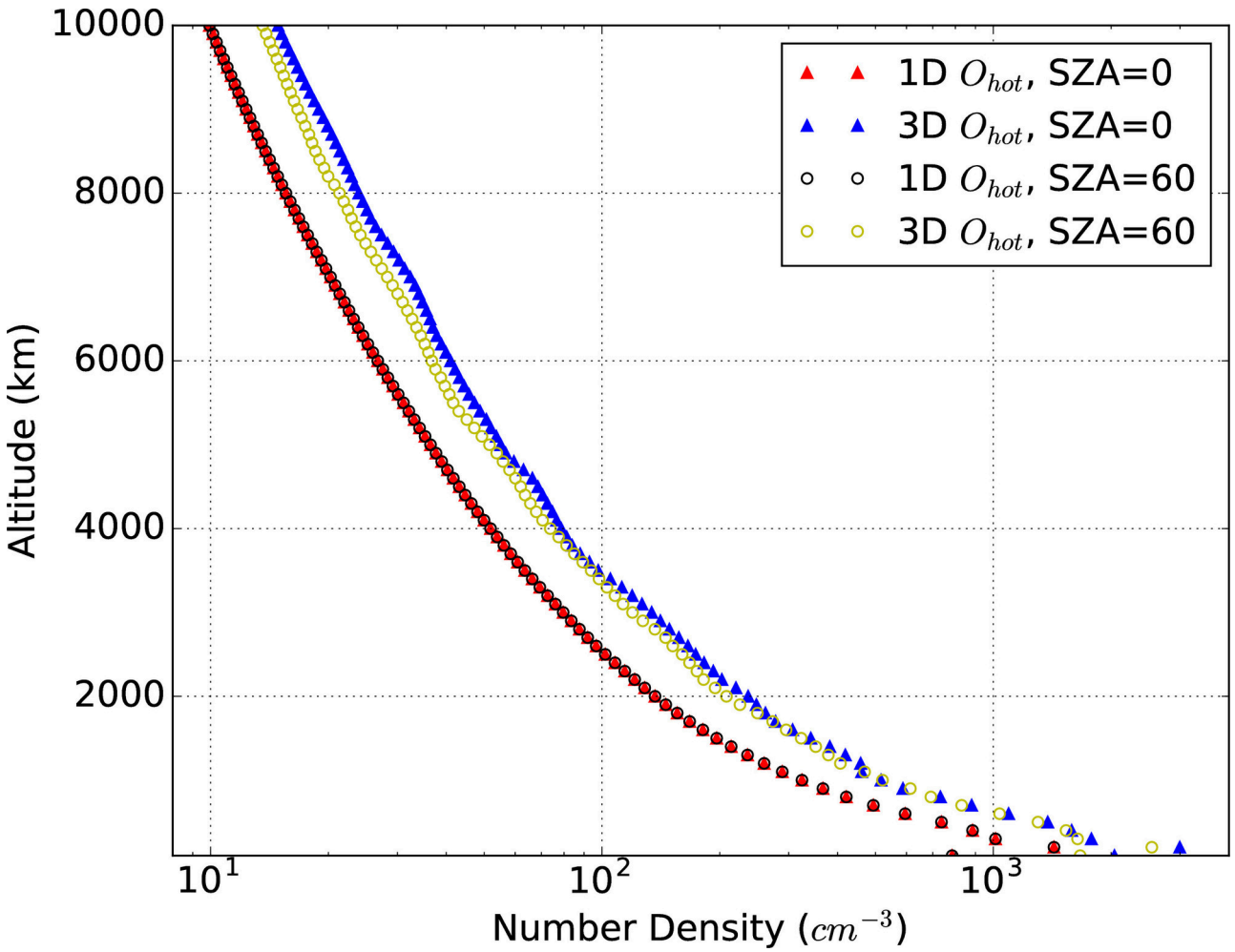

2018ja025543-f09-z-.eps

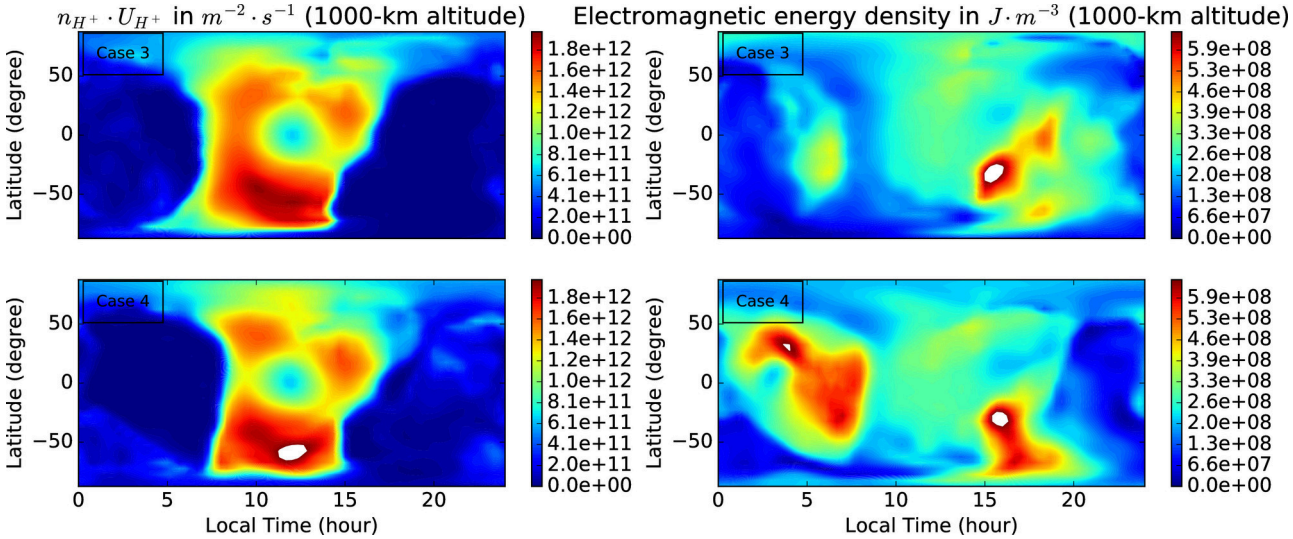

2018ja025543-f10-z-.eps